DESY 94-204
November 1994

ISSN 0418-9833

New Results from HERA

on Photoproduction and Diffraction, the Proton Structure Function, Deep Inelastic Scattering at Low x, Heavy Flavour Production, Jets and Searches for Leptoquarks

presented at the
27th International Conference on High Energy Physics, Glasgow
20 - 27 July 1994

by

Members of the ZEUS Collaboration

F. Barreiro [1], S. Bhadra[2], M. Lancaster[3] , J.N. Lim[4], S. Söldner-Rembold[5] and B. Straub[6]

1. Universidad Autónoma de Madrid, Spain
2. York University, Toronto, Canada, and DESY, Hamburg, Germany
3. University of Oxford, Oxford, U.K.
4. McGill University, Montreal, Canada
5. Freiburg University, Freiburg, Germany
6. Columbia University, New York, U.S.A.

List of contributed papers by the ZEUS collaboration covered by the speakers of this report

1. Measurement of the proton structure function F_2 from the HERA 1993 ep data
   (ICHEP94 0711)
2. Properties and cross section of diffractive events produced in deep inelastic ep scattering at HERA
   (ICHEP94 0660)
3. Observation of vector meson production in electron-proton DIS at HERA
   (ICHEP94 0663)
4. Observation of jet production in deep inelastic scattering with a large rapidity gap at HERA
   (ICHEP94 0666)
5. Search for excited fermions in electron-proton collisions at HERA
   (ICHEP94 0667)
6. Search for leptoquarks in electron-proton collisions at HERA
   (ICHEP94 0669)
7. Study of neutral strange particle production in deep inelastic scattering at HERA
   (ICHEP94 0670)
8. Cross section measurement of the process $ep \rightarrow epJ/\Psi$ at HERA
   (ICHEP94 0672)
9. Observation of D* production in ep collisions at HERA
   (ICHEP94 0673)

10. Two-jet production in deep inelastic scattering neutral current events at HERA and a search for a resolved photon contribution
(ICHEP94 0674)

11. Multi-jet production in deep inelastic ep scattering at HERA
(ICHEP94 0676)

12. Comparison of energy flows in deep inelastic scattering events with and without a large rapidity gap
(ICHEP94 0678)

13. Measurement of two-jet cross sections in photoproduction at HERA
(ICHEP94 0682)

14. Inclusive jet differential cross sections in photoproduction at HERA
(ICHEP94 0683)

15. Study of the photon remnant in resolved photoproduction at HERA
(ICHEP94 0684)

16. Observation of hard scattering in photoproduction events with a large rapidity gap at HERA
(ICHEP94 0686)

17. Measurement of the elastic ρ^0 photoproduction cross section at HERA
(ICHEP94 0688)

18. Inclusive transverse momentum distributions of charged particles in diffractive and non-diffractive photoproduction at HERA
(ICHEP94 0690)

19. Observation of photoproduction of ϕ-mesons at HERA
(ICHEP94 0691)

20. Initial study of leading neutrons in ep collisions at HERA
(ICHEP94 0692)

21. First measurements with the ZEUS leading proton spectrometer
(ICHEP94 0693)

New results on DIS at low x from ZEUS

Fernando Barreiro

Universidad Autónoma de Madrid, Spain

On behalf of the ZEUS Collaboration

Abstract

I summarize the most important results obtained to date by the ZEUS Collaboration on Deep Inelastic Scattering (DIS) at low x. The main emphasis is on a discussion of events with a Large Rapidity Gap (LRG), their main characteristics, jet structure, energy flow and exclusive vector meson production. Particular attention is paid to the interpretation of these events as due to the scattering on pointlike constituents of a colourless object in the proton: the pomeron.

1. Introduction

In the Quark Parton Model (QPM), DIS is understood to proceed via the exchange of a current which is subsequently absorbed by a quark in the proton, giving rise to final states consisting of the scattered lepton, the struck quark and the diquark remnant. Multihadronic final states are the result of the fragmentation of the colour string joining the current quark with the proton remnant. QCD corrections to the next order in perturbation theory are given by QCD Compton and Boson Gluon Fusion (BGF) processes. Since the probability to find valence quarks in the proton tends to zero as the Bjorken variable x goes to the kinematic limits i.e. 0 and 1, BGF processes are expected to be dominant at low x values. In Fig. 1 we show a textbook example of an event as expected in the QPM. In addition to the scattered electron and the current jet a continuous energy flow stretching from the jet axis to the proton direction is observed. In contrast, no energy flow is observed between the current jet to the scattered electron.

One of the most important results obtained at HERA so-far, has to do with the strong rise of the cross section or F_2 at low x. There are two sources of this strong rise. On the one hand, quark pair production via the so-called BGF discussed previously.

Because of the configuration in colour space, hadrons

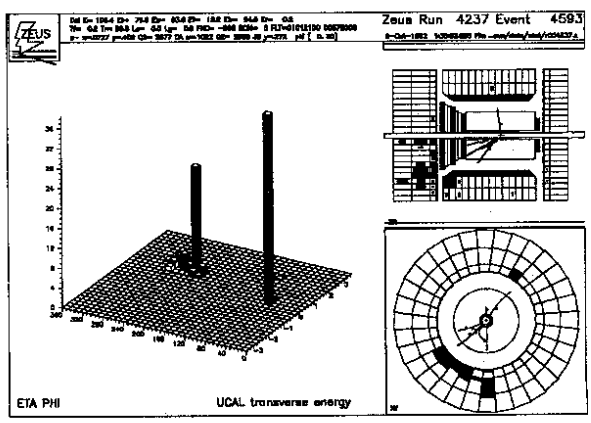

Figure 1. A DIS event as expected in the QPM

are produced along the two strings joining the quark (antiquark) with the diquark (resp. quark which emitted the gluon) in the proton. Hadrons thus fill the complete phase space in pseudorapidity. In contrast, we have found at low x a new class of events which are characterized by a large rapidity gap (LRG).

They are interpreted to proceed via the exchange of a colourless object in the proton: the pomeron (P). In the process $\gamma^* P \rightarrow q\bar{q}$, hadrons will be the result of the

‡ E-mail: F35FER@DHHDESY3

fragmentation of only one string i.e. that connecting the quark and the antiquark, thus giving rise to a void between the proton and one of the final state partons. Since the calorimeter in the proton direction covers up to pseudorapidity values of 4.3 units, selecting events with $\eta_{max} \leq 1.5$, where η_{max} is defined as the pseudorapidity of the calorimeter cell with energy deposit in excess of 400 MeV closest to the proton beam direction, is tantamount to requiring events with a rapidity gap larger than 2.8 units.

Although diffractive processes have been studied for 30 years now, their true nature is far from being understood. In particular the connection with the usual calculational techniques in strong interaction physics, namely QCD, is still missing, both in the perturbative as well as in the non-perturbative regimes. We have used two models to make comparisons with our data and thus get into a deeper understanding of these processes. One model follows the original idea of Ingelman and Schlein [1], acording to which one introduces parton densities in the pomeron in the same way as one introduces parton densities in a hadron. Thus the cross sections for diffractive ep collisions will be the result of convoluting a pomeron flux in the proton vertex, given by Regge phenomenology, with the cross section for $\gamma - parton$ two body scattering. This model has been coded in a Monte Carlo program, POMPYT, by P. Bruni and G. Ingelman [2]. The parton densities in the pomeron can be chosen and varied at will. We have used two parameterizations, which are proportional to $(1-z)^5$, soft, and $z(1-z)$, hard. The latter is in accord with the original proposal by Donnachie and Landshoff [3]. As an alternative we have used a Monte Carlo, written by A. Solano [4], of the Nikolaev-Zakharov model [5]. In this model one considers quantum fluctuations of the virtual photon into $q\bar{q}$ and $q\bar{q}g$ final states which subsequently interact with the pomeron perturbatively. In lowest order the pomeron is considered to be a two-gluon system. In this model one arrives at an effective quark density in the pomeron which lies somewhere in between the two previously discussed.

2. Experimental setup and data selection

The data presented here have been taken with the ZEUS detector [7] operating at HERA, the $e-p$ collider at DESY (Hamburg, Germany). I will restrict myself to the 1993 data taking period, where the integrated luminosity collected by the experiment amounted to 550 nb^{-1}. We select DIS events by looking for scattered electron candidates using the pattern of energy deposition in the calorimeter. The electron energy was required to be larger than 5 GeV. The efficiency for finding isolated electrons in this energy range was greater than 97%. Restricting ourselves to $Q^2 \geq 10\ GeV^2$ and $y \geq 0.04$ we select a sample of 38192 events which is found to be free from beam-gas and photoproduction background [8]. Our data populates a region in the Q^2, x plane which extends two orders of magnitude above (below) that covered by previous fixed target experiments [6].

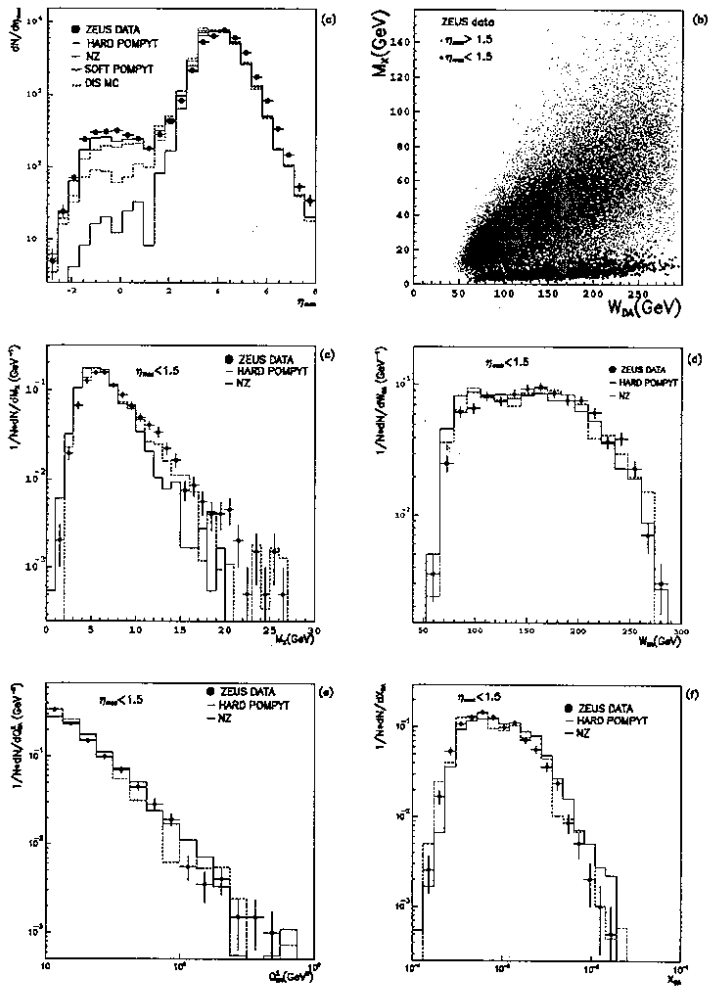

Figure 2. General characteristics of DIS LRG events

3. Events with a LRG, general characteristics

The distribution in η_{max} for the DIS sample is shown in Fig. 2a. Notice that the data exhibit a tail which is an order of magnitude above the expectations in the standard model Monte Carlo LEPTO. The shape of this tail is properly described by the Nikolaev Zakharov model as well as by POMPYT with a hard parton density. In fact, one can fit the η_{max} distribution to the linear sum of the expectations in DIS and diffractive scattering. Depending on the model used for the latter we obtain for the relative diffractive contribution $12.0 \pm 1.8\%$ and $9.2 \pm 1.5\%$

for Nikolaev-Zakharov and hard POMPYT respectively. Incidentally, soft POMPYT cannot describe the shape of the η_{max} distribution.
Figs. 2b-f show relevant distributions in the mass of the hadronic system, W, Q^2 and Bjorken x. Again Monte Carlo models of the type described above give a rough description of the main characteristics exhibited by these large rapidity gap events.

If we interpret these LRG events as due to pomeron exchange one can calculate the fraction of the proton momentum carried by the pomeron, ξ, using the simple relation $\xi = \frac{M_X^2+Q^2}{M_X^2+W^2}$. In Fig. 3 one can see how events with a LRG defined as $\eta_{max} \leq 1.5$ saturate the tail in ξ. The average value for these events being 3.2×10^{-3} corresponding to an average pomeron momentum of $2.6\ GeV$.

Since we cannot yet tag on forward going protons

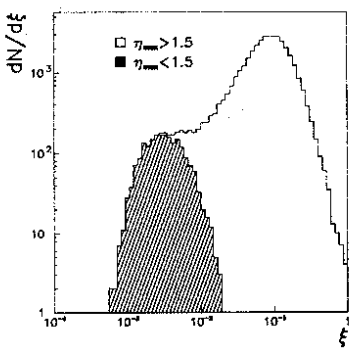

Figure 3. The pomeron fractional momentum

and thus cannot determine the t distribution associated with the proton vertex for which there exist clear predictions in Regge theory, we try to find indirect evidence that LRG events are due to pomeron exchange. It is instructive to look at the ratio r of large rapidity gap events to all DIS events as a function of W, Fig. 4a. This ratio is found to be constant for W values in excess of 140 GeV where our acceptance is large and W independent. We consider this as further evidence that LRG events are due to pomeron exchange. It is equally interesting to look at the ratio of LRG events to all DIS events as a function of Q^2 for various x bins, Fig.4b-d. We find this ratio to be Q^2 independent. Thus, LRG events exhibit the same scaling violation effects as normal DIS events. If LRG events are interpreted as due to pomeron exchange our data suggest that we are scattering on a pomeron pointlike constituent.

4. Jet structure in events with a LRG

If the interpretation discussed so far were correct then we should be able to observe jet production in events with a LRG. We look for jets in pseudorapidity-azimuth space using the cone algorithm. We perform the search both in the laboratory as well as in the $\gamma^* - p$ c.m. system. In the latter, a cluster is called a jet when the transverse energy collected in a cone of radius unity (with the metric $R = \sqrt{(\Delta\eta^2 + \Delta\phi^2)}$), is larger than 2 GeV.

We find the fractions of 1-, 2- and 3-jet events to be

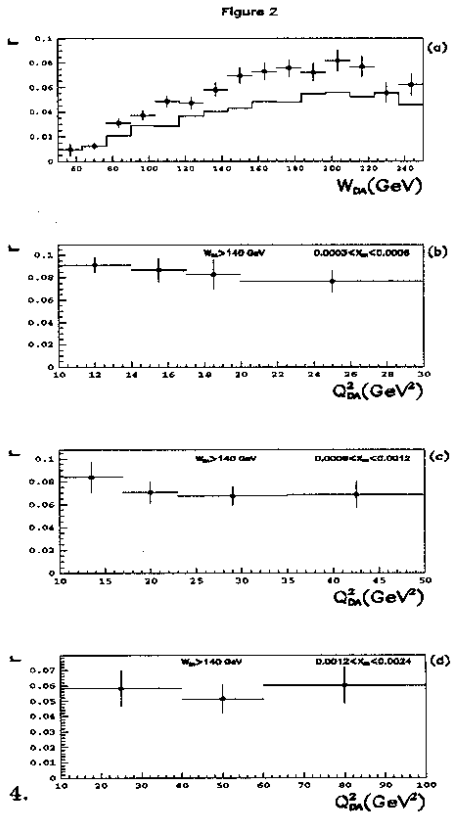

Figure 4.

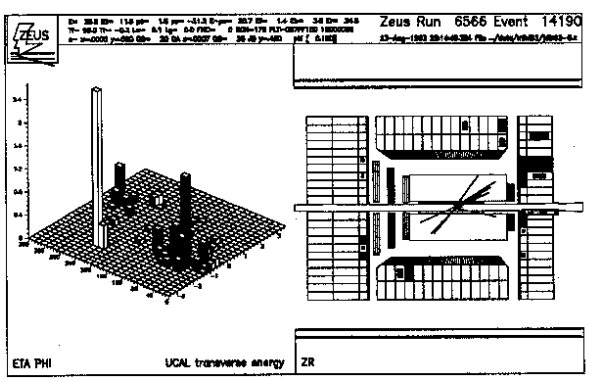

Figure 5. A diffractive two-jet event

$5.9 \pm 0.5\%$, $3.5 \pm 0.4\%$ and $0.4 \pm 0.1\%$. Most important we find that the tail of the hadronic transverse energy distribution is saturated by events with multijet structure, Fig. 6a. Thus, as in in any other collider process, there is an underlying $2 \rightarrow 2$ scattering responsible for diffraction. As also shown in Fig. 6 the two jets are produced back-to-back in the transverse plane and the jet transverse energies reach values up to approximately

10 GeV. In Fig. 5 we show one such event where one

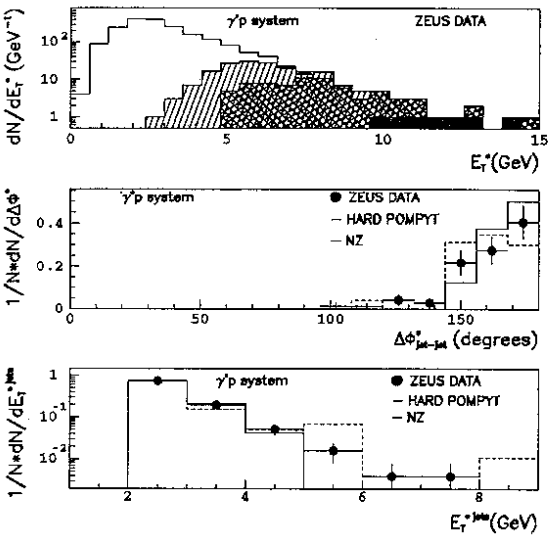

Figure 6. Characteristics of diffractive two-jet events

can clearly see the scattered electron, two jets and no trace of the proton remnant.

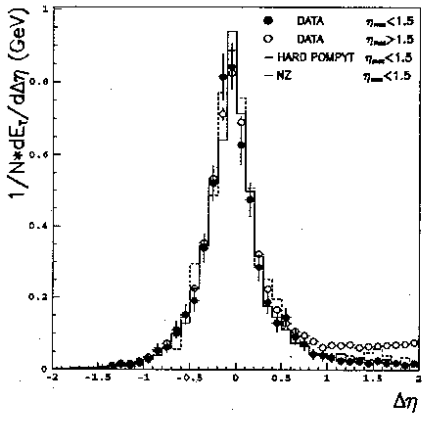

Figure 7. Jet profiles for DIS events with and without LRG

It is illustrative to look at the energy flow around the jet axis for jet events in the LRG sample. One can clearly see, Fig. 7, that in addition to the central jet core, both tails tend to zero no matter whether you move from the jet axis towards the electron or proton directions., in agreement with the hard POMPYT or NZ Monte Carlo programs.
Fig. 7 also illustrates that the absence of colour flow between the jet axis and the proton direction is not a consequence of the selection criteria, as exemplified by the jet profiles in the normal DIS sample where we demanded that the jets be produced at negative pseudo-rapidities. Furthermore the jet core is very similar for DIS events with and without a LRG.

5. Energy flow in events with a LRG

The same conclusions reached in the preceeding section can be obtained from a comparative study of the energy flow in DIS events with and without a LRG, i.e. without restriction to those events with jet structure [9].
The main results are summarized in Fig. 8 where

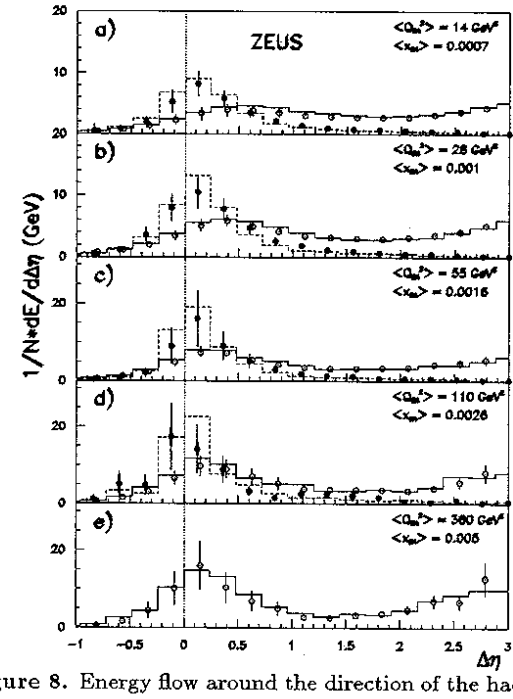

Figure 8. Energy flow around the direction of the hadronic system

we show the corrected energy flows for the two classes of events discussed above. The correction procedure based on standard Monte Carlo techniques is done in such a way that the origin is made to coincide with the direction of the struck parton. Events with and without LRG exhibit marked differences. For the former the position of the peak is shifted towards positive values, with the shift becoming less pronounced as Q^2 increases. Substantial energy flow is observed for large $\Delta\eta$ values. For the latter, however, the position of the peak is independent of Q^2 and well centered at zero, with furthermore negligible energy flow at large $\Delta\eta$ values.

6. Exclusive vector meson production

Just as in e^+e^- annihilation one distinguishes between omnia and production in the continuum, it is also appropiate when discussing diffraction not only to concentrate on hadron production in the continuum, see preceeding sections, but also to consider exclusive vector meson production. The relative rates for ρ, ϕ, J/Ψ, Υ as well as their production characteristics will in the future be a fertile testing ground for PQCD calculations. Again

present available statistics allow us to present only the results of our investigation on the lowest lying vector meson state, i.e. the ρ. They are summarized in Fig. 9. For $7 \leq Q^2 \leq 10\ GeV^2$, we obtain a cross-section for $\gamma^* p \rightarrow \rho^0 p$ of $123 \pm 15(stat) \pm 39(syst)\ nb$ to be compared with the Brodsky et al. calculation of 165 nb [10].

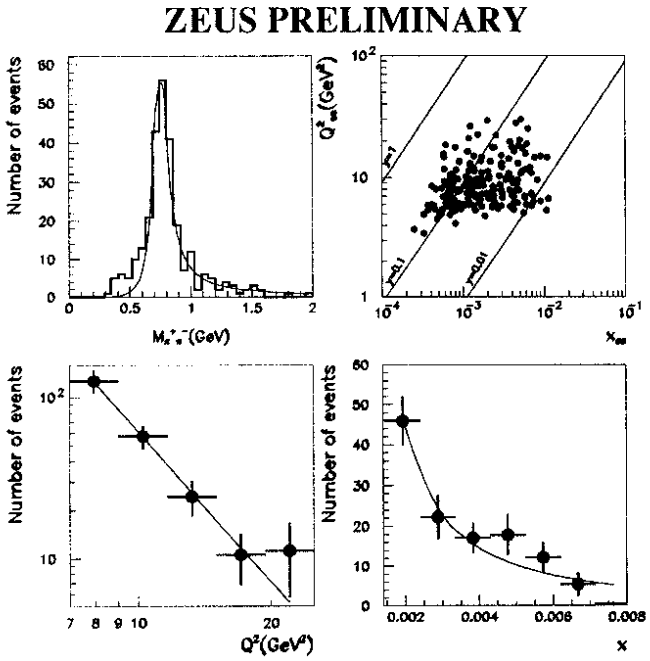

Figure 9. The Q^2 and x dependence of ρ production

7. Strange particle production

One of the main differences between the two models for diffraction that we have been discussing so far has to do with the heavy quark content of diffractive events. In the Nikolaev Zakharov model, heavy quark production is strongly suppressed as a consequence of the uncertainty principle. Fluctuations of the virtual photon into heavy quark pairs are characterized by much smaller transverse sizes. Present statistics preclude an analysis of the charm content of events with a LRG. We have to restrict ourselves, for the time being, with an investigation of the strangeness content of DIS events with and without a LRG. The results are summarized in Fig. 10 where we show the transverse momenta and pseudorapidities of the neutral kaons in both samples along with comparisons with Monte Carlo expectations. Clearly more statistics is needed to be able to discriminate between different models.

8. Conclusions

Approximately 10% of the DIS events with $Q^2 \geq 10\ GeV^2$ are of a diffractive nature. If interpreted as due to pomeron exchange we find that the average pomeron momentum is 2.6 GeV. Diffractive events exhibit the same scaling violations as normal DIS events. The natural interpretation is that we are scattering on pointlike constituents in the pomeron, as corroborated by our observation of multijet structures in DIS LRG events. From the point of view of low x physics, HERA experiments can be considered as fixed target experiments, our stationary target being a colorless object in the proton, the pomeron. More statistics is needed to unravel its true nature.

Acknowledgements This report was written while visiting Oxford University under the exchange program between the Ministery of Education, Spain, and the Royal Society, London. Their support is gratefully acknowledged. I would like to thank Drs. L. Labarga and J. Terrón as well as my graduate students J.M. Hernandez and J. Puga for help in the preparation of the manuscript.

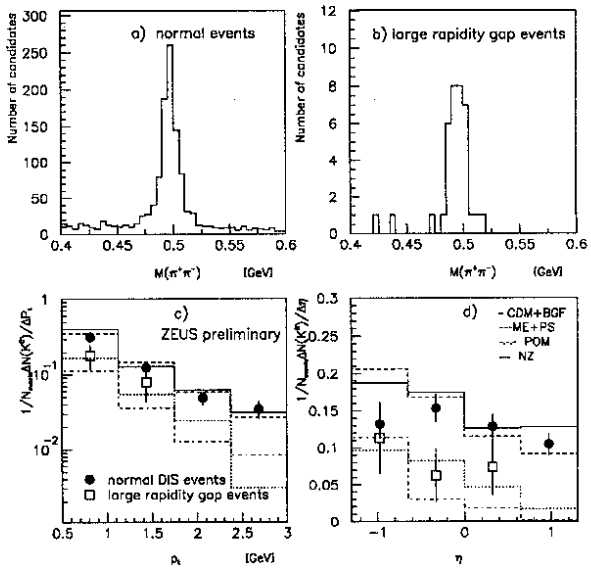

Figure 10. Neutral kaon transverse momentum and pseudorapidity in DIS with and without LRG

References

[1] G. Ingelman and P. Schlein, Phys. Lett. **B152** (1985) 256.
[2] P. Bruni and G. Ingelman, *DESY 93-187.*
[3] A. Donnachie and P.V. Landshoff, Phys. Lett. **B191** (1987) 309.
[4] A. Solano, *Ph. D. Thesis, University of Torino, unpublished.*
[5] N.N. Nikolaev and B.G. Zakharov,Zeit. Phys. **C53** (1992) 331.
[6] M. Lancaster, *these proceedings.*
[7] ZEUS Coll., M. Derrick *et al.*, Phys. Lett. **B315** (1993) 481
[8] ZEUS Coll., M. Derrick *et al.*, Phys. Lett. **B332** (1994) 228
[9] ZEUS Coll., M. Derrick *et al.*, DESY 94-117.
[10] S.J. Brodsky *et al.*, SLAC-PUB-6412.

Photoproduction and Diffraction at HERA

Sampa Bhadra

York University, Department of Physics, 4700 Keele Street, Toronto, Canada, and
Deutsches Elektronen Synchrotron, Notkestrasse 85, 22603 Hamburg, Germany.
(on behalf of the ZEUS and H1 collaborations)

Abstract

Results from photoproduction at HERA are presented, including cross section measurements for ρ^0, ϕ, and J/ψ production. We have found jets which are a signature for hard scattering processes. An analysis of two-jet events allows us to probe the structure of both the photon and the proton. Comparisons are made of di-jet production to predictions from LO QCD, using different structure functions of the proton and photon. We have searched for hard scattering in diffractive events and compared our results to models where the exchanged pomeron is composed of partons.

1. Introduction

The gauge interactions of the electron and photon are well known, but the interaction of the photon with hadrons or photons is less well understood. HERA is an electron (26.7 GeV) - proton (820 GeV) collider. However, the large flux of quasi-real photons ($Q^2 \approx 0$) from the electrons makes it an ideal machine to explore the nature and structure of the photon. The average centre of mass energy $W_{\gamma p} \approx 200$ GeV is a factor of ten higher than in previous experiments. Hence it is interesting to compare our results [1] to theoretical models which are sensitive to the high energy behaviour, since pre-HERA predictions vary widely.

An excellent review by Storrow [2] brings some order to the varied and sometimes confusing classification of photon interactions. The classification is made in terms of the P_t scale, where "low P_t" is the region where the differential cross section is well described by an exponential behaviour in P_t. This soft physics is non-perturbative and not presently calculable in QCD. The subprocesses contributing are elastic, inelastic diffractive, and non-diffractive. The slope in P_t at larger values is more like a power law, and in this region of hard scattering, we can use perturbative QCD to describe the scattering process. The photon interacts directly, or resolves itself before interacting. One important distinction between photons and hadrons is that photons can interact directly with the partons of the proton, while hadrons only interact through their constituent partons.

The fractional momentum x_γ (x_p) carried by the parton in the photon (proton) can be written as

$$x_\gamma = \frac{E_t^1 e^{-\eta_1} + E_t^2 e^{-\eta_2}}{2E_\gamma}, x_p = \frac{E_t^1 e^{\eta_1} + E_t^2 e^{\eta_2}}{2E_p} \quad (1)$$

where E_γ (E_p) is the photon (proton) energy, E_t^1, E_t^2 refer to the transverse energies, and η_1, η_2 to the pseudorapidities of the outgoing partons. The direct component, where all the energy of the photon enters the reaction, has $x_\gamma = 1$, while the resolved component will result in a value less than 1. We use the variables x_γ and x_p to probe the quark and gluon content of the photon and proton.

2. Cross section measurements of ρ^0, ϕ, J/ψ

Photoproduction results from the 1992 and 1993 data taking period of HERA have been obtained from about 25 nb^{-1} and 500 nb^{-1} of data, respectively. The photoproduction triggers for ZEUS required calorimetric energy to be deposited in the rear (photon)

direction, and were of two types:
a.) "tagged"; requiring the detection of the scattered electron at very small angles, thereby limiting Q^2 to less than 0.02 GeV^2 and
b.) "untagged"; with no requirement on the detection of the scattered electron, but with energy deposition in the rear direction and the detection of at least one charged track. This allows the direct reconstruction of the photoproduced vector mesons decaying into charged track states. The offline requirement of the absence of a detected scattered electron in the main rear calorimeter limits Q^2 to less than 4 GeV^2.

The total "tagged" photoproduction cross sections $\sigma(\gamma p)_{tot}$ at HERA for the 1993 data [3],[4] are shown in Fig 1, for $W_{\gamma p} \approx 200$ GeV. Also shown (solid circles) are lower energy measurements [5]. Global event characteristics are used by ZEUS to obtain the fraction of non-diffractive, inelastic diffractive, and elastic components to be 64.0%, 23.3%, and 12.7% respectively. Assuming that 82% of the elastic cross section is due to ρ^0 production yields an indirect measurement of the elastic cross section $\sigma(\gamma p \rightarrow \rho^0 p)$ to be 14.8 $\pm$5.7 μb, and this is shown in Fig 1.

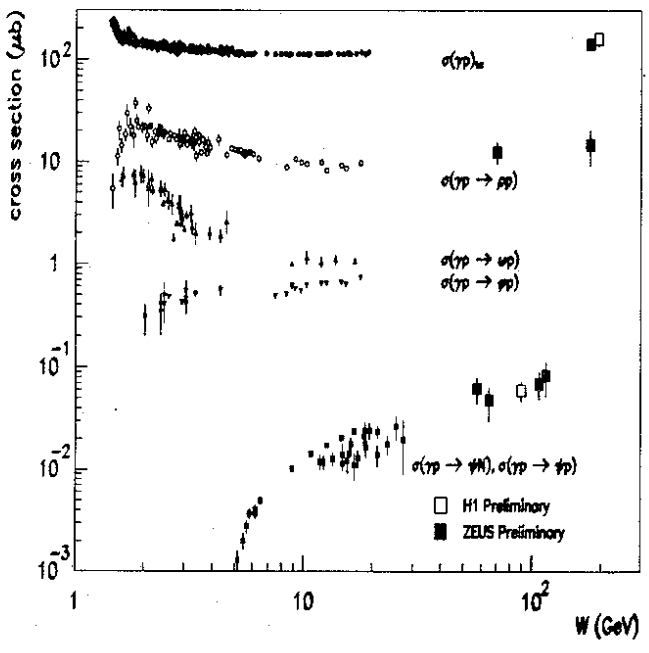

Figure 1. Photoproduction cross section measurements from HERA and lower energy experiments.

The direct measurement of the ρ^0 elastic cross section has been obtained by ZEUS from the "untagged" trigger at $60 < W_{\gamma p} < 80$ GeV. Two well reconstructed tracks of opposite charge coming from a good vertex are required, and an invariant mass is formed by assuming these two tracks to be pions. Events in which neutral particles are produced are rejected by requiring that there be less than 200 MeV in any calorimeter cell outside a limited region around the track direction.

Proton diffraction is a serious background, and in the absence of a fully equipped leading proton spectrometer, we require that there be less than 1 GeV in the forward calorimeter (i.e. the proton direction). Demanding $0.55 < m_{\pi\pi} < 1.0$ GeV reduces the contamination from other vector mesons. Finally, we limit the ρ^0 transverse momentum squared to be less than 0.5 (GeV/c)^2 to further reduce the proton diffraction contamination.

The mass spectrum is shown in Fig 2. The deviation from a Breit-Wigner shape for the ρ^0 is well known, and is caused by the interference (dashed-dotted) of the resonant $\pi^+\pi^-$ production (dotted) and a non-resonant background (dashed). A functional form of the three contributions is used to extract the resonant contribution to the cross section. The result is $\sigma(\gamma p \rightarrow \rho^0 p) = 12.5 \pm 0.7(stat) \pm 2.8(syst)$ μb, and is shown in Fig 1, where lower energy data (open circles) are also shown for comparison [5].

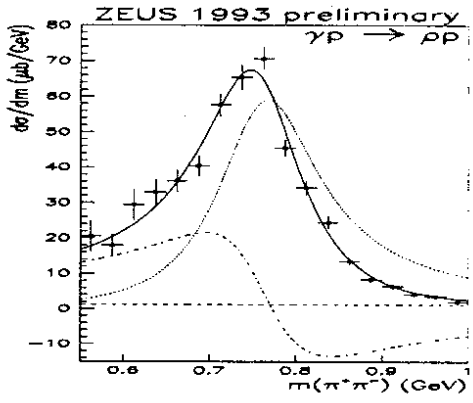

Figure 2. Invariant mass distribution of $\pi^+\pi^-$.

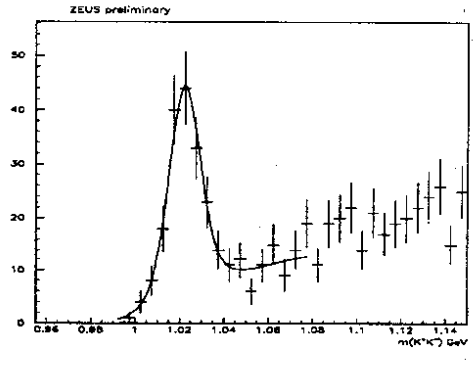

Figure 3. Invariant mass distribution of K^+K^-.

ZEUS has performed a similar analysis to obtain a

measurement of the elastic ϕ cross section for the decay channel ($\phi \rightarrow K^+K^-$). The invariant mass distribution is shown in Fig 3. However, the cut on the ϕ transverse momentum squared is $0.2 < P_t^2 < 1.0$ (GeV/c)^2, as the acceptance drops sharply below 0.2 (GeV/c)^2 due to the geometry of the detector and the trigger. The average acceptance in the selected region is 20%. The elastic cross section $\sigma(\gamma p \rightarrow \phi p)$ within this restricted range in $W_{\gamma p}$ and P_t^2 is measured to be $278 \pm 30(stat) \pm 78(syst)$ nb.

The investigation of the photoproduction of heavy quarks is a probe of strong interaction physics in a region characterised by the transition between perturbative QCD and non-perturbative interactions. The photoproduction of J/ψ is an ideal process to explore this regime. A clear signal can be seen from H1 in Fig 4 from the invariant mass distribution of the sum of the electron and muon decay modes of J/ψ. The analysis for the measurement of $\sigma(\gamma p \rightarrow (J/\psi)p)$, where $J/\psi \rightarrow e^+e^-$ or $\mu^+\mu^-$, is covered elsewhere in these proceedings, but the results are shown in Fig 1 for H1 and ZEUS, along with lower energy data [5].

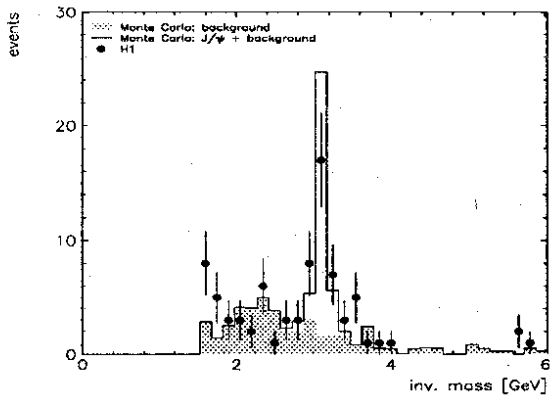

Figure 4. Invariant mass distribution of e^+e^- and $\mu^+\mu^-$.

3. Inclusive transverse momentum distributions

Photon diffractive events are characterised by a gap in rapidity between the leading particle and the photon dissociated system of mass M_x, where the reaction is mediated by the exchange of a pomeron [6] having the quantum numbers of the vacuum. Detectors being installed in the very forward region will tag the recoiling proton for an unambiguous classification of diffractive events. The final implementation of these detectors is still in progress, and hence not used in this analysis.

The tagged data sample has been divided into diffractive and non–diffractive subsets, according to the pseudorapidity † η_{max} of the most forward calorimeter deposit with energy above 400 MeV. We have found that a cut on $\eta_{max} < 2.0$ is very effective in separating the diffractive events from non-diffractive events.

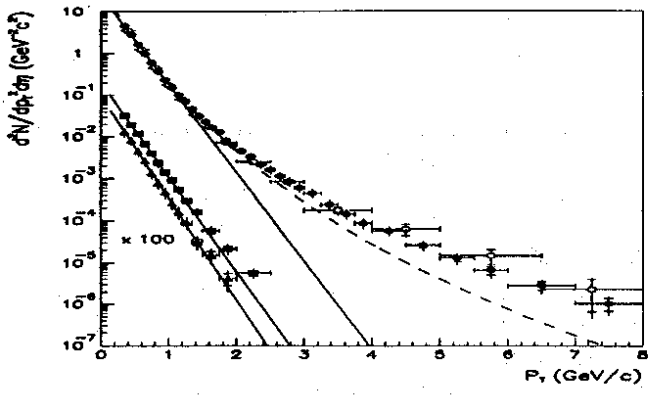

Figure 5. Transverse momentum distribution of charged tracks for photoproduction events.

The spectrum of transverse momenta P_t of tracks satisfying stringent quality criteria in diffractive events is shown in Fig 5, where the data are displayed in two different M_x bins: triangles for $\langle M_X \rangle = 5$ GeV, squares for $\langle M_X \rangle = 10$ GeV. Here M_x is the relevant energy scale for the interaction. Exponential fits (solid lines), normalised to the data points below 1.2 GeV/c, shows that the diffractive data points are consistent with such a fit.

The non-diffractive events are shown in the same figure for H1 (open circles,[7]) and ZEUS (solid circles). The dashed curve is a power law fit to UA1 [8] data for $p\bar{p}$ collisions at a centre of mass energy of 200 GeV. Although is not clear at what energies the comparison should be made, it is clear that the HERA data at similar energies have a harder spectrum. This is hardly surprising since, although the photon exhibits hadron-like properties, the parton distributions in the photon and proton are different, and also because the photon interacts directly.

4. Hard Scattering in Photoproduction

A deviation from the "soft" exponential term in Fig 5 is an indication of hard interactions, and searching for jet structure is the next step, as jets are the observable objects most closely related to the partons. Both H1 and ZEUS have found jets in photoproduction events with transverse energy greater than 5 GeV. The partonic definition of x_γ in Eqn. 1 is redefined to refer to the variables measured from the jets.

Both ZEUS and H1 have evidence for the direct and resolved components in photoproduction through the variable x_γ, as seen from the distribution of x_γ

† $\eta = -log(tan(\theta/2))$, where the polar angle is with respect to the proton direction.

from the ZEUS data in Fig 6. Monte Carlo simulations are also shown for the resolved (dashed) and direct (dotted) contributions, and the sum (solid line). The operational definition used for the photon classification is that $x_\gamma < 0.75$ is "resolved" and $x_\gamma > 0.75$ is "direct".

At HERA, events with two observable jets ($E_T^{jet} \gtrsim$ 6 GeV, $\eta^{jet} \lesssim 2$) are sensitive to x_p as low as 10^{-3} and x_γ of approximately 10^{-1}. We consider jets at nearly equal pseudorapidities, with an average of $\bar{\eta}$, as the configuration of "same-side" jets allows very small x values of the initial partons to be examined [9].

The differential cross section in $\bar{\eta}$ for $x_\gamma > 0.75$ is dominated by direct photon interactions and so is insensitive to the parton distribution in the photon, but sensitive instead to the gluon distribution in the proton. This is shown in (Fig 7a) (solid circles) and compared to LO QCD calculations using various parton distribution sets for the proton. Low-x effects such as non-zero k_T of the incoming partons may explain why the measured cross section lies below most curves at low $\bar{\eta}$ [10]. However, other higher order or hadronisation corrections have not yet been fully considered.

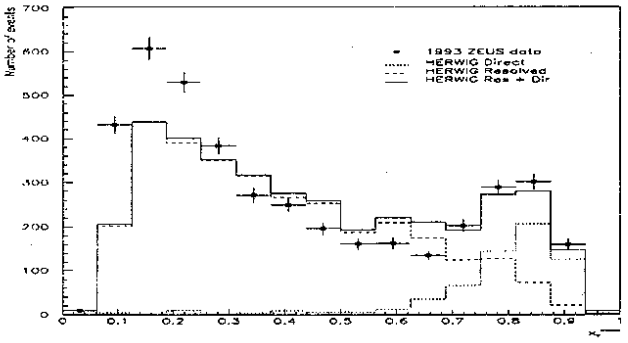

Figure 6. x_γ distribution for data and HERWIG Monte Carlo with direct and resolved components

The region $x_\gamma < 0.75$ is sensitive to the gluon distribution in the photon. As the x_p values probed here are in the region where the parton densities of the proton are well constrained by other measurements, the sensitivity to different parton distribution sets in the proton is small as can be seen from a comparison of MRSA in Fig 7b and GRV (LO) in Fig 7c. However, the sensitivity to different photon parton distribution sets is large as c ıe variations in the predictions. Higher order QCD calculations are necessary before strong conclusions can be drawn.

5. Hard Diffraction in Photoproduction

The observed properties of the diffractive cross section have been described by Regge theory, where the process

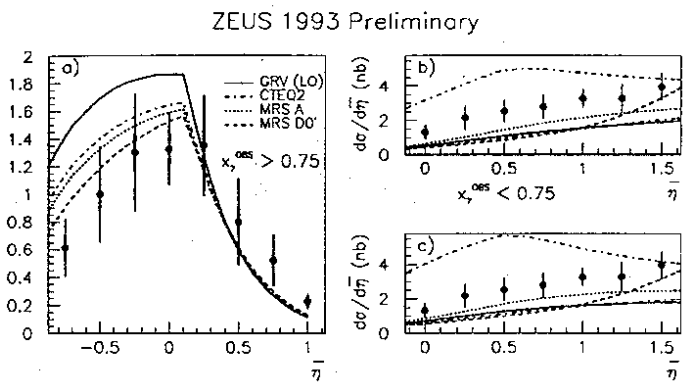

Figure 7. $\bar{\eta}$ distribution for $x_\gamma > 0.75$ is shown in fig a.). GS2 set was used for the photon, and the sets for the parton distribution for the proton were: GRV (solid line), CTEQ2 (dash-dotted line), MRSA (dotted line) and (MRSD0)' (dashed line). In fig b.) and c.), $x_\gamma < 0.75$ and the parton distributions for the photon are LAC3 (high, dash-dotted line). GS2 (dotted line), GRV (solid line), LAC1 (dashed line), and DG (low, dash-dotted line). The parton distribution for the proton was MRSA for fig b.) and GRV (LO) for fig c.).

proceeds through the exchange of the pomeron. The interplay of Regge theory and perturbative QCD is one motivation for studying hard scattering in diffractive processes [11], since these subjects are mostly without experimental overlap. In one such treatment of this subject [12], Ingelman and Schlein have modelled the pomeron as a hadron having constituent partons. The result of hard interactions is the production of jets, similar to the discussion in section 4. Monte Carlo programs modelling a partonic interaction of the pomeron and based on pQCD now exist, (e.g. POMPYT [13]) and we can confront these with HERA diffractive data.

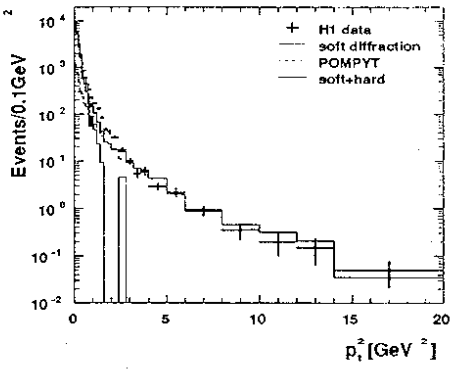

Figure 8. Square of the transverse momentum distribution for photoproduction diffractive events from H1.

Fig 8 shows the transverse momentum squared for diffractive events selected with $\eta_{max} < 1.5$, from H1 data [14]. PYTHIA, which models soft diffraction, cannot account for the high P_t^2 tail, but POMPYT,

which models hard diffraction, reproduces this hard tail well, which could be an indication of hard partonic scattering in photon diffraction events.

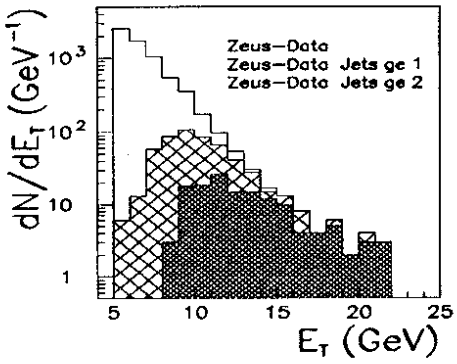

Figure 9. Transverse energy of diffractive events from ZEUS for all events with E_t greater than 5 GeV (solid line), and the subset with at least one jet (crossed) , and greater than one jet (shaded).

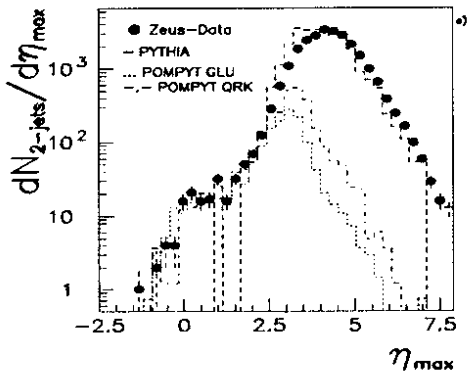

Figure 10. η_{max} for all γp events with two jets from ZEUS.

It is natural to search for jet structure in such diffractive events. Fig 9 shows the transverse energy E_t spectrum for diffractive events with $E_t > 5$ GeV, and we see that 6.5% (2.1%) of the events have at least one (or more) jet(s). Jet production dominates the high E_t region, with jets having E_t as large as 10 GeV being observed.

To verify that this is not the tail of the non-diffractive data, we show in Fig 10 the η_{max} distribution for photoproduction events with two jets in ZEUS. The excess of jets for η_{max} below 1.5 is not reproduced by photoproduction processes as modelled in PYTHIA, which predicts less than 0.1% of events with jets in this region, to be compared to the 0.63% seen. However, POMPYT, with hard interactions from a quarkonic (QRK) or gluonic (GLU) pomeron, gives a reasonable agreement in this region. These observations are consistent with hard partonic scattering in diffractive γp collisions.

The restriction on η_{max} imposes a limit in the range of phase space available for large masses and large E_t jets which are desirable for more conclusive studies of the hard interactions. We will cleanly identify diffractive events with the final implementation of the Leading Proton Spectrometers and the Forward Neutron Calorimeters in H1 and ZEUS. Already, ZEUS has detected fully measured $\gamma p \rightarrow \rho^0 p$ events. High energy leading neutrons have also been observed for the first time. In addition to the diffractive processes, reactions from a pion exchange with the production of a forward neutron will also be investigated. The study of forward baryonic states will be an important aspect of the future physics programs at HERA.

6. Conclusions

We have reported on a wide range of physics results from photoproduction at HERA, from cross section measurements to detailed studies of the elastic and inelastic diffractive subprocesses. The large centre of mass energy of HERA has allowed the observation of the direct and resolved components of the photon interaction, and jets as evidence for hard scattering. We have found evidence of hard partonic scattering in diffractive γp collisions. With the final implementation of the forward detectors, we will be able to identify and explore the characteristics of high mass diffractive events.

7. Acknowledgements

We thank the DESY directorate for their strong support and encouragement. The remarkable achievements of the HERA machine group were essential and are appreciated. The author appreciates the time and effort invested by several H1 and ZEUS members during the preparation of this talk.

References

[1] Contributed papers to this conference ICHEP Ref 672,682,686,688,690,691,692,693.
[2] J.K. Storrow. J. Phys, G19 (1993) 1641.
[3] H1 Collaboration, Phys Lett. B 299 (1993) 374.
[4] ZEUS Collaboration, Zeit.Phys. C63 (1994) 391.
[5] A. Baldini et. al., Landolt-Bornstein, Group I, Vol 12b, Springer-Verlag, ed. H.Schopper.
[6] K. Goulianos, Phys. Rep. 101 (1983) 169.
[7] H1 collaboration, Phys. Lett.B328 (1994) 176.
. . . . . al., Nucl. Phys. B335 (1990) 261.
[9] J. R. Forshaw and R. G. Roberts, Phys. Lett. B319 (1993) 539.
[10] J. R. Forshaw and R. G. Roberts, Phys. Lett. B335(1994) 494.
[11] E. Berger et. al., Nucl Phys. B286 (1987) 704.
[12] G. Ingelman and P. Schlein, Phys. Lett. B152 (1985) 256.
[13] P. Bruni and G. Ingelman, DESY 93-187.
[14] S. Levonian, Proceedings on the Workshop on Two-Photon Physics at LEP and HERA, Lund, May 1994, 96.

A measurement of the proton structure function $F_2(x, Q^2)$ at low-x and a determination of the low-x gluon distribution

Mark Lancaster†

Department of Nuclear & Particle Physics,
University of Oxford
Keble Road, Oxford, OX1 3RH, UK

On behalf of the ZEUS Collaboration

Abstract

A measurement of the proton structure function $F_2(x, Q^2)$ by the ZEUS detector at HERA from data taken during the 1993 running period is described. Results are presented for $7 < Q^2 < 10^4$ GeV^2 and x values as low as 3×10^{-4}. The F_2 values are used to extract the gluon distribution at $Q^2 = 20$ GeV^2 for x down to 8×10^{-4} using both published approximate methods and a global NLO fit to the ZEUS data at low-x combined with NMC data at larger x. A substantial rise in the gluon density and F_2 is found at small x in comparison with previous results obtained at larger values of x.

1. Introduction

The large centre of mass energy available at HERA allows measurements of the proton structure function to be made for x values as small as 10^{-4} for $Q^2 \gtrsim 7$ GeV^2. The data sample used corresponds to an integrated luminosity of 0.54 pb^{-1} and represents a twenty fold increase over that used in the first ZEUS measurement of F_2 [1]. Two independent analyses have been performed, one using our standard double angle approach and the other based on the energy and angle of the scattered electron. The size of the systematic errors in the double angle method has been reduced in comparison to our previous measurement through the increased statistics and improved understanding of the performance of the detector. The improved precision of the F_2 data has allowed the gluon distribution to be determined from a full NLO QCD fit.

† E-mail: lancaster@vxdesy.desy.de

2. ZEUS detector

ZEUS is a multipurpose detector that has been described elsewhere [2]. The principal detector components for the F_2 analysis are the inner tracking detectors and the high resolution uranium-scintillator calorimeter (CAL) [4]. The inner tracking detectors [3] operating in a magnetic field of 1.43T provide a vertex resolution of 4 mm in z, which compares to the width of the vertex distribution (determined by the proton bunch length) of 11 cm. The CAL is divided into three parts, forward, barrel and rear (FCAL,BCAL and RCAL) with each part subdivided into towers which in turn are subdivided longitudinally into electromagnetic (EMC) and hadronic (HAC) sections. The sections are subdivided into cells, each of which is viewed by two photomultiplier tubes. Under test beam conditions the CAL has an energy resolution, in units of GeV, of $\sigma_E = 0.35\sqrt{E}$(GeV) for hadrons and $\sigma_E = 0.18\sqrt{E}$(GeV) for electrons. The CAL also provides a time resolution of better than 1 ns for energy deposits greater than 4.5 GeV, which is used

for background rejection. Luminosity information is obtained through the detection of quasi-elastic $ep \to ep\gamma$ events in two lead scintillator calorimeters placed 35 and 107 m downstream of the main detector [5]. Non-ep backgrounds are rejected by veto detectors downstream of the interaction point (IP).

3. Deep inelastic kinematics

Structure functions are expressed as functions of the variables Bjorken x and Q^2. Because the ZEUS detector is almost hermetic the kinematic variables x and Q^2 can be constructed in a variety of ways using combinations of electron and hadronic system energies and angles [6]. The ability to measure x and Q^2 in different ways offers a powerful systematic check on the resulting F_2 values. In this F_2 analysis two methods have been used to measure x and Q^2 : firstly the electron method where the kinematics are reconstructed from the energy (E'_e) and angle (θ'_e) of the scattered electron and secondly the double angle (DA) method in which only the angles of the scattered electron (θ'_e) and the hadronic system (γ_H) are used, which reduces the sensitivity to energy scale uncertainties. In the naïve quark-parton model γ_H is the scattering angle of the struck quark. In the double angle method in order that the hadronic system is well measured it is necessary to ensure a minimum of hadronic activity in the CAL away from the beam pipe. A suitable quantity for this purpose is the hadronic estimator of the variable y [7], defined by, $y_{JB} = \Sigma_h \frac{(E-P_z)}{2E_e}$ where E_e is the electron beam energy and the z axis points in the direction of the proton beam.

4. Event selection and backgrounds

Data were collected with a trigger comprising of three levels. Deep inelastic scattering (DIS) events are selected at the first level using a logical OR of three conditions on sums of energy in the EMC calorimeter cells. At the second level using cuts based on the event times measured in the FCAL and RCAL and at the third level using cuts on the quantity δ, where $\delta \equiv \Sigma_i E_i(1-\cos\theta_i) > 20$ GeV $- 2E_\gamma$ and E_i, θ_i are the energy and polar angle (with respect to the nominal IP) of calorimeter cells and E_γ is the energy measured in the photon calorimeter of the luminosity monitor. For fully contained events $\delta \sim 2E_e = 53.4$ GeV. For events from photoproduction processes δ peaks at low values; this is because the scattered electrons remain within the rear beam pipe and the bremsstrahlung spectrum is soft. Additionally at the third level tighter event time cuts and cuts to remove halo-muons and cosmics are applied.

The overall trigger acceptance after all three levels is above 95% independent of x and Q^2 in the ranges of interest for this analysis. The 2×10^6 events recorded by the trigger are subject to final selection cuts. For the DA method the following cuts are employed : $E'_e > 5$ GeV, $y_e < 0.95$, $y_{JB} > 0.04$, $35 < \delta < 60$ and the impact point of the electron on the face of the RCAL be outside a square of 32 cm centred on the beam axis. For the electron analysis the E'_e cut is raised to 8 GeV and the y_{JB} cut removed since the need to reconstruct γ_H accurately is removed. The distribution of the events after the DA selection cuts is shown in figure 1 along with the bins used for the analysis. The bin sizes at low Q^2 ($Q^2 \lesssim 100$ GeV^2) are determined by resolution whilst for high Q^2 they are determined by statistics. Non-ep backgrounds are statistically subtracted and total $< 1\%$. The predominant ep background arises from photoproduction events where a photon in the final state fakes an electron in the detector. The low δ values of photoproduction events in comparison to DIS events allow the background to be estimated from a fit to the δ spectrum. The results of the fit were cross checked with a photoproduction Monte-Carlo. The total photoproduction background was 2.5% and was predominantly concentrated at high-y where the largest background in any one bin was 12%.

5. F_2 extraction

For the bins used in this analysis the Z_0, F_L and radiative corrections are small such that the Born cross section can be expressed as :

$$\frac{d^2\sigma}{dxdQ^2} = \frac{2\pi}{xQ^4} F_2(1+(1-y)^2)(1+\Delta_{Z_0}+\Delta_{F_L}+\Delta_r).$$

The F_2 extracted is a pure photon exchange F_2. The effects of the Δ_i corrections, acceptance and event migration are corrected for using an event sample generated using the HERACLES [8] Monte- Carlo. The hadronic final state was simulated using the colour-dipole model [9] incorporating boson-gluon fusion as implemented in ARIADNE [10] for the QCD cascade, and JETSET [11] for the hadronisation. The detector simulation is based on the GEANT [12] program. The systematic errors were calculated by varying selection cuts and the analysis methods (see [13] for further details). The systematics are typically large at small-y ($\sim$ 20%) where uncertainties in the determination of γ_H dominate and at large-y ($\sim$ 10%) due to background and electron identification uncertainties. The F_2 values as a function of x for Q^2 values ranging from 8.5 to 2000 are shown in figure 2 along with the F_2 values calculated using some current parton distribution parameterisations. A clear rise in F_2 is seen which persists to large values of Q^2 in contrast to the predictions of parton distributions which embody a flat gluon distribution as a function of x for example the MRSD$'_0$ [14] parameterisation. The ZEUS F_2 values

are found to satisfy a compact parameterisation of the form :

$$F_2 = [(1-x)(1+x)]^4(0.35 + Bx^{(C+Dlog_{10}Q^2)}),$$

where $B = 0.0170 \pm 0.0041$; $C = -0.352 \pm 0.023$ and $D = -0.155 \pm 0.015$.

6. Determination of the gluon density

The gluon momentum density $xg(x,Q^2)$ is related only indirectly to F_2 through the QCD scaling violations expressed in terms of the Altarelli-Parisi equation [15] :

$$\frac{dF_2(x,Q^2)}{d\ln Q^2} = \frac{\alpha_s(Q^2)}{2\pi}\left[\int_x^1 \frac{dz}{z}\left(\frac{x}{z}\right)P_{qq}\left(\frac{x}{z}\right)F_2(z,Q^2) + 2\sum_q e_q^2 \int_x^1 \frac{dz}{z}\left(\frac{x}{z}\right)P_{qg}\left(\frac{x}{z}\right)zg(z,Q^2)\right],$$

where the sum runs over all active quark flavours and e_q is the charge of quark q, $\alpha_s(Q^2)$ is the strong coupling constant and P_{qq}, P_{qg} are the quark and gluon splitting functions. The gluon term in the above equation dominates the scaling violations at low-x. Two approaches have been used to extract the gluon density at $Q^2 = 20$ GeV^2 from the ZEUS F_2 data. Firstly two approximate methods, Prytz [16] and EKL [17], have been used in which the gluon distribution is expressed directly in terms of the measured quantities : F_2 and $dF_2/d\ln Q^2$ and secondly from a full NLO QCD fit to the ZEUS F_2 data along with larger-x F_2 data from NMC [18]. The F_2 scaling violations are shown in figure 3 along with the straight line fits used to determine the F_2 and $dF_2/d\ln Q^2$ values necessary as input to the approximate methods. The full NLO QCD fit is also shown in the figure. The NLO fit takes the functional form for the singlet, valence, non-singlet and gluon distributions from the MRS parameterisations [14]. In particular a gluon distribution of the form : $xg(x,Q_0^2) = A_g x^{\delta_g}(1-x)^{\eta_g}$ is used. The parameters for the valence distributions are taken directly from MRSD'_ . From the fit a value of $\delta_g = 0.35$ at $Q^2 = 7$ GeV^2 is found. The results of the fit and the two approximate methods are shown in figure 4. The systematic errors shown in the figure were evaluated by repeating the analysis but using F_2 values offset by each of the systematic errors which in combination form the total F_2 systematic error. Included in the systematic error of the fit is the uncertainty due to the relative normalisation of the ZEUS ($\pm 3.5\%$) and NMC ($\pm 1.6\%$: 90 GeV data, $\pm 2.6\%$: 280 GeV data) data sets. In addition to the statistical and systematic errors shown in the figure there are additional theoretical errors. An error of $\sim 6\%$ due to the uncertainty in α_s is present in both approaches. Moreover the assumptions of the Prytz and EKL methods lead to further systematic uncertainties. The Prytz method overestimates the gluon distribution since it neglects the quark contribution to the scaling violations, however it is relatively insensitive to the assumed shape of the gluon distribution. In contrast the EKL method is found to be very sensitive to the assumed x distribution of F_2 and the gluon. An x variation for F_2 and the gluon distribution of the form : $x^{-\omega_0}$ is assumed. Reasonable variations in the value of ω_0 i.e. $0.3 < \omega_0 < 0.5$ cause a 40% change in the extracted gluon distribution. For the NLO fit the effects of : valence quark parameterisation, strange quark content, quark mass, higher twist contributions were all investigated and found to be negligible. The treatment of the charm threshold was found to have a small ($\lesssim 5\%$) effect. The gluon shows a steep increase at low x in comparison to previous results obtained at larger values of x.

References

[1] ZEUS Collab., M. Derrick et al., Phys. Lett. B316 (1993) 412.
[2] ZEUS Collab., M. Derrick et al., Phys. Lett. B293 (1992) 465.
[3] C.B. Brooks et al., Nucl. Instr. Meth. A283 (1989) 477; B. Foster et al., Nucl. Instr. Meth. A338 (1994) 254; C. Alvisi et al., Nucl. Instr. and Meth. A305 (1991) 30.
[4] A. Andresen et al., Nucl. Inst. and Meth. A309 (1991) 101; A. Bernstein et al., Nucl. Inst. and Meth. A336 (1993) 23; A. Caldwell et al., Nucl. Inst. and Meth. A321 (1992) 356.
[5] K. Piotrzkowski, PhD Thesis University of Cracow 1993, DESY F35D-93-06 (1993).
[6] S. Bentvelsen, J. Engelen and P. Kooijman, Proceedings of the Workshop 'Physics at HERA' vol. 1, DESY 1992, 23; S. Bentvelsen, PhD Thesis University of Amsterdam 1994.
[7] F. Jacquet and A. Blondel, Proceedings of the study of an *ep* facility for Europe, DESY 79/48 (1979) 391, U. Amaldi ed.
[8] HERACLES 4.1: A. Kwiatkowski, H. Spiesberger and H.-J. Möhring, Proceedings of the Workshop 'Physics at HERA' vol. 3, DESY 1992, 1294; A.Kwiatkowski, H.Spiesberger and H.-J.Möhring, Z. Phys. C50 (1991) 165.
[9] B. Andersson et al., Z. Phys. C43 (1989) 625.
[10] ARIADNE 3.1: L. Lönnblad, Comput. Phys. Commun. 71 (1992) 15.
[11] JETSET 6.3: T. Sjöstrand, Comput. Phys. Commun. 39 (1986) 347; T. Sjöstrand and M. Bengtsson, Comput. Phys. Commun. 43 (1987) 367.
[12] GEANT 3.13: R. Brun et al., CERN DD/EE/84-1 (1987).
[13] ZEUS Collab., M. Derrick et al., DESY 94-143 (1994), submitted to Z. Phys. C.
[14] A.D. Martin, R.G. Roberts and W.J. Stirling, Phys. Lett. B306 (1993) 145; Phys. Lett. B309 (1993) 492 (erratum).
[15] V.N. Gribov and L.N. Lipatov, Sov. J. Nucl. Phys. 15 (1972) 438, 675; L.N. Lipatov, Sov. J. Nucl. Phys. 20 (1974) 181; G. Altarelli and G. Parisi, Nucl. Phys. 126 (1977) 297.
[16] K. Prytz, Phys. Lett. B311 (1993) 286; K. Prytz, RAL-94-036 (1994).
[17] R.K. Ellis, Z. Kunszt and E.M. Levin, Fermilab-PUB-93/350-T, ETH-TH/93/41.
[18] NMC Collab., P. Amaudruz et al., Phys. Lett. B295 (1992) 159.

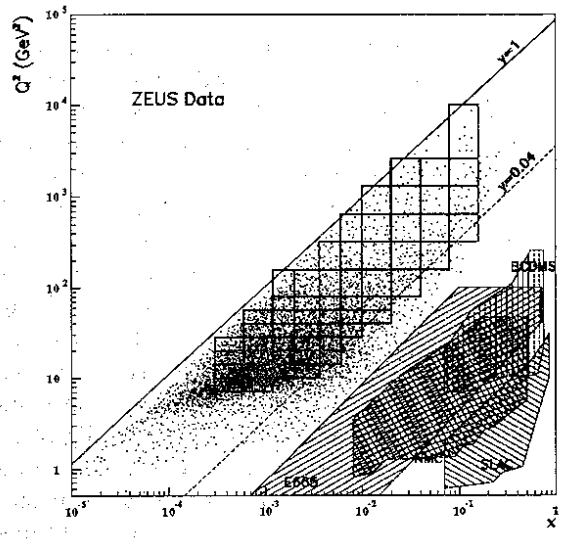

Figure 1. The x-Q^2 distribution of the ZEUS F_2 event sample and the bins used in the analysis. The x-Q^2 regions where fixed target F_2 measurements have been made are also shown.

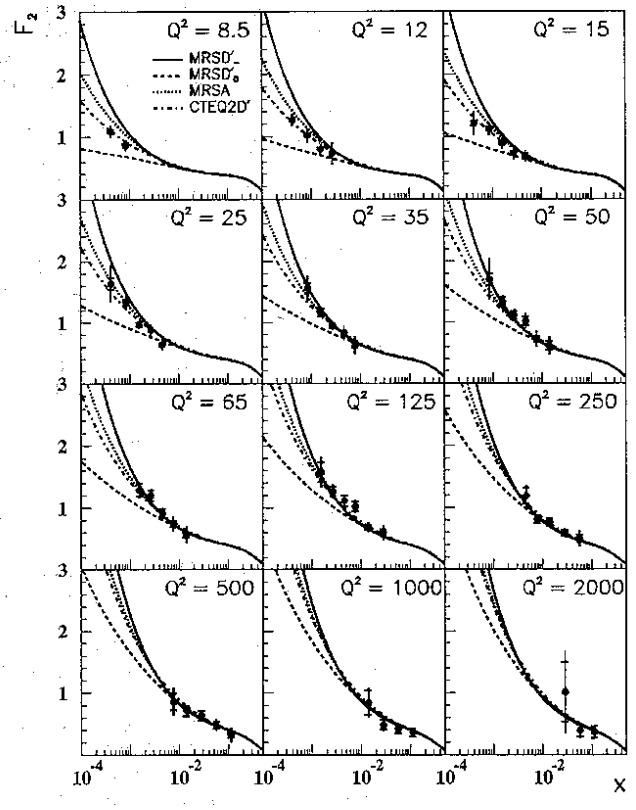

Figure 2. ZEUS 1993 final F_2 values (solid circles) plotted as functions of x at fixed Q^2 and compared to the following recent PDF calculations: MRSD'_ (full curve), MRSD$'_0$ (dashed curve), CTEQ2D' (dash-dotted curve) and MRSA (dotted). The inner error bar shows the statistical error and the full bar the statistical and systematic errors added in quadrature. Q^2 is measured in GeV^2. The overall normalisation uncertainty of 3.5% is not included.

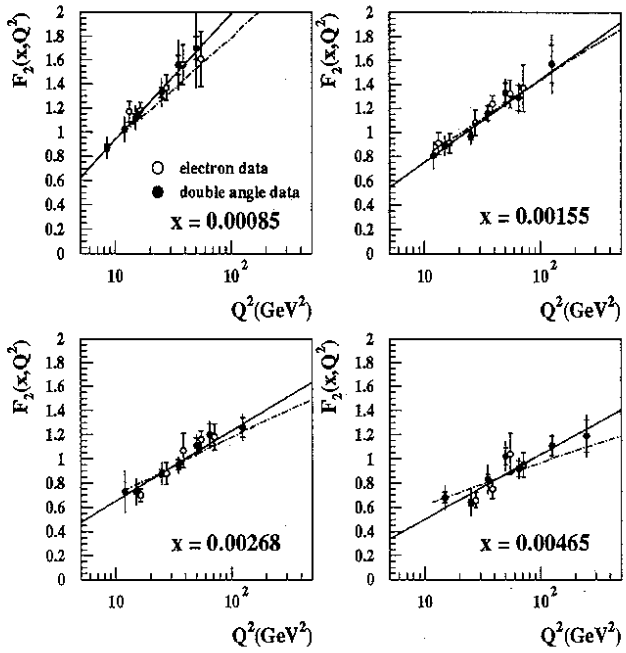

Figure 3. The F_2 structure function measurements of ZEUS together with the linear fits (solid lines), and the result from the global NLO fit, (dashed-dotted lines). The error bars show the statistical (inner error) and systematic error added together in quadrature.

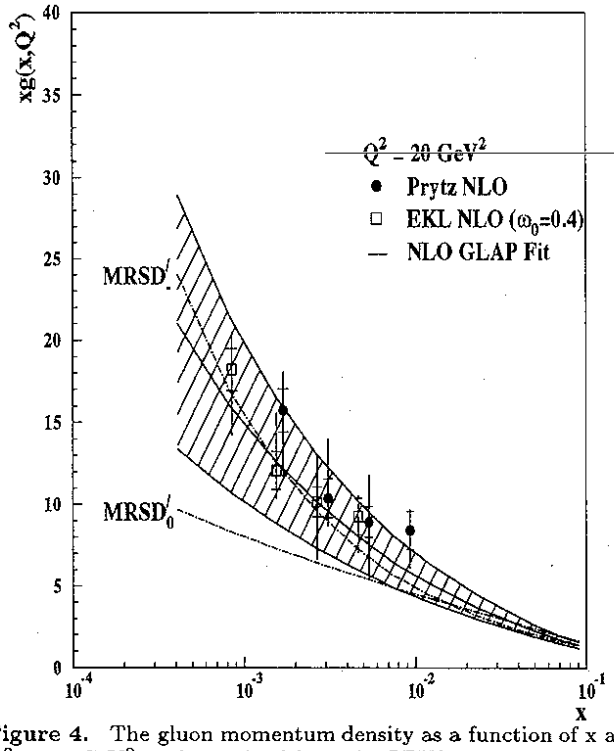

Figure 4. The gluon momentum density as a function of x at $Q^2 = 20\ GeV^2$ as determined from the ZEUS data with Prytz and EKL in NLO. The error bars show the experimental statistical (inner error) and systematic error added to together in quadrature. The solid line shows the result of the NLO GLAP global fit with the associated error indicated by the hatched region. The gluon parameterisations of MRSD'_ and MRSD$'_0$ are shown as dash-dotted lines.

Cross Section Measurement of D^* and Elastic J/ψ Production at HERA

J N Lim ‡

McGill University, Dept. of Physics,
Montreal, Quebec, Canada

On behalf of the ZEUS collaboration

Abstract

This paper reports on the first observation of charmed mesons in the decay channel $D^{*+} \rightarrow (K^-\pi^+)\pi^+$ (+ c.c.) and a preliminary measurement of the cross section of D^* and elastic J/ψ production at HERA using the ZEUS detector.

1. Introduction

We search for $c\bar{c}$ production at HERA by looking for the fragmentation products of the heavy flavour quarks which produce a $D^{*\pm}$ and give a preliminary cross section measurement for D^* production using 486 nb^{-1} of data taken in 1993. The method relies on the kinematic constraints of the decay $D^{*+} \rightarrow D^0\pi^+$. The momentum of the pion coming from the D^* is 40 MeV in the D^* rest frame, giving a mass difference $\Delta M(M(D^0\pi) - M(D^0))$ of 145.42 MeV [1] which can be measured accurately. The D^0 is detected via the $D^0 \rightarrow K^-\pi^+$ (+c.c.) channel. Background from $b\bar{b}$ pairs is very small and we assume all the D^* events originated directly from charm quarks.

We also present preliminary results of the cross section measurement of J/ψ in photoproduction in the reactions $ep \rightarrow eJ/\psi p$. The photon-proton center of mass energy ($W_{\gamma^* p}$) is confined to the kinematic region where the detector acceptance is well understood and the process is properly simulated. The present data sample contains photoproduction events with $Q^2 < 3$ GeV^2.

‡ E-mail: lim@vxdesy.desy.de.

2. The ZEUS Detector

The ZEUS [2] detector has been described elsewhere. The components relevant to this analysis are the vertex and central-tracking detectors, the uranium-scintillator calorimeter, the barrel and rear muon detectors, the veto wall detector, a scintillator counter (C5) detector to veto beam-gas interactions and the luminosity monitor.

3. Monte Carlo Simulation

The Monte Carlo programs HERWIG [3] and PYTHIA [4] were used to model the expected hadronic final states in $c\bar{c}$ production. Elastic J/ψ production was simulated with the DIPSI[5] and the EPJPSI[6] generators.

4. D^* Reconstruction and Results

Pairs of oppositely charged tracks with transverse momentum, $p_T > 0.5$ GeV, were combined and considered in turn to be a kaon or a pion. The combination was accepted as a possible D^0 candidate if the $K\pi$ invariant mass lay between 1.80 and 1.90 GeV. To reconstruct D^* mesons, these D^0 candidates were combined with an additional track having $p_T > 0.16$ GeV and opposite charge to that of the kaon. No

particle identification was used in this analysis. A cut of $p_T(\mathrm{D}^*) > 1.7\,\mathrm{GeV}$ was applied to reduce background and the pseudorapidity, $\eta = -\ln[\tan(\frac{\theta}{2})]$, was confined to the region, $|\eta(\mathrm{D}^*)| < 1.5$, where the detector is well understood.

Figure 1 shows the ΔM signal with a peak at 145.5 ± 0.2 MeV and width of $1.0 \pm 0.2\,\mathrm{MeV}$. There are 74 ± 14 D^* events observed over a background of ~ 40 events. The $M(\mathrm{K}\pi)$ distribution for events with $142 < \Delta M < 149$ MeV is shown in figure 2. The fit gives a D^0 mass of 1.85 ± 0.01 GeV, with a width of $\sim$ 20 MeV and 72 ± 13 events.

The ΔM distribution was used to estimate the number of D^* events over the background. The efficiency was evaluated using both PYTHIA and HERWIG Monte Carlo with different structure function parametrisations. The total systematic error on the results was estimated to be 19 %.

For the kinematic range $p_T(\mathrm{D}^*) > 1.7\,\mathrm{GeV}$ and $|\eta(\mathrm{D}^*)| < 1.5$ we obtained $\sigma(ep \rightarrow \mathrm{D}^{*+}X + c.c.)B(\mathrm{D}^{*+} \rightarrow \mathrm{D}^0\pi^+ \rightarrow (\mathrm{K}^-\pi^+)\pi^+) = 1.5 \pm 0.3(stat) \pm 0.3(syst)\,\mathrm{nb}$.

Extrapolation outside the selected kinematic range, assuming different parton density parametrisations and a branching ratio $B(c \rightarrow \mathrm{D}^{*+} \rightarrow \mathrm{D}^0\pi^+ \rightarrow (\mathrm{K}^-\pi^+)\pi^+)$ of 7.1×10^{-3} [7], gave a total charm cross section of $\sigma(ep \rightarrow c\bar{c}X) \sim 1.7\,\mu\mathrm{b}$ for MRSD-[8]/LAC1[9] and $\sim 1\,\mu\mathrm{b}$ for MRSD- with either GRV[10],ACFGP[11] or DG[12].

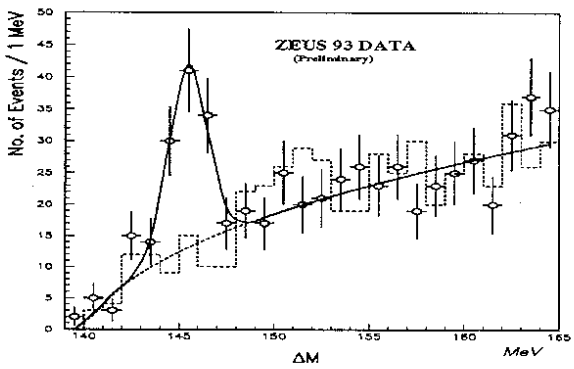

Figure 1. ΔM distribution for $p_T(\mathrm{D}^*) > 1.7$ GeV and $|\eta(\mathrm{D}^*)| < 1.5$. The dashed line is the plot for the wrong charge combinations.

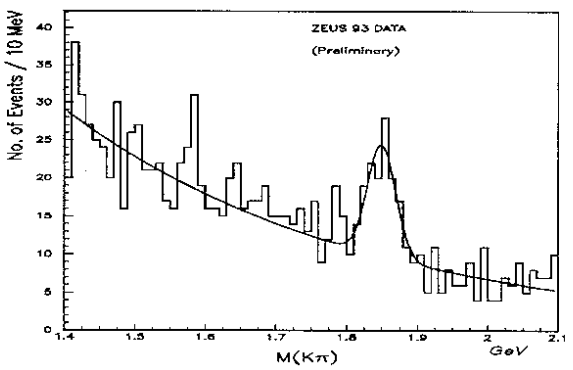

Figure 2. $K\pi$ invariant mass distribution for those candidates with $(142 < \Delta M < 149)$ MeV in the whole range of $M(K\pi)$. The fit consists of a gaussian plus an exponential background shape.

5. J/ψ Event Selection and Results

The J/ψ was identified in its leptonic decay modes. In the case of the muon channel, particle identification was accomplished by matching at least one of the final state tracks with calorimeter energy deposits corresponding to a minimum ionising particle and to matching hits in the muon detectors. Electron identification was accomplished by matching final state tracks to calorimeter energy deposits consistent with that of an electron.

Events with exactly two well reconstructed tracks within $|\eta| < 1.5$ and transverse momenta greater than 0.5 GeV were accepted. In addition, the total energy in the calorimeter, apart from the energy deposited by the two lepton candidates from the J/ψ decay, was required to be less than 1.0 GeV. This criterion was imposed to select elastic events i.e., from the reaction $ep \rightarrow e\mathrm{J}/\psi\mathrm{p}$, by ensuring that there was no other activity in the detector. These selection criteria, however, do not exclude the events where the proton dissociates diffractively and remains undetected in the beampipe.

The invariant mass spectra, displayed in figure 3, were then fitted with a Gaussian form and a polynomial background. The fitted mass for the J/ψ candidates was 3.03 ± 0.02 GeV with a width of 80 ± 16 MeV in the electron channel, and 3.07 ± 0.02 GeV, with a width of 66 ± 12 MeV, for the muon channel, respectively. In the case of the electron channel, the shift of the fitted mass of the J/ψ from the nominal J/ψ mass (3.1 GeV) is attributed to energy loss in the material encountered by the electrons. This was also observed in the Monte Carlo. A fit which included a bremsstrahlung function gave a mass of 3.07 ± 0.02 GeV.

The selected range of $\mathrm{W}_{\gamma^*\mathrm{p}}$ was 40 GeV $< \mathrm{W}_{\gamma^*\mathrm{p}} <$ 140 GeV, where the observed acceptance on the average was well above 10%. A preliminary estimate of the systematic uncertainties was 21% for the electron and 30% for the muon channel. The photoproduction cross section, σ_{γ^*p}, is related to the electron proton cross section by a flux factor given by the Equivalent Photon Approximation [13]. The photoproduction cross sections, the integrated photon flux used in these calculations, and the electroproduction cross sections, σ_{ep}, are summarized in table 1. The photoproduction cross sections as a function of $\mathrm{W}_{\gamma^*\mathrm{p}}$ are shown in figure 4 which includes earlier J/ψ measurements [14].

$W_{\gamma^* p}$ (GeV)	40-140	
channel	e^+e^-	$\mu^+\mu^-$
Int. Luminosity (nb^{-1})	496	490
acceptance	25.2%	17.7%
signal events	58 ± 9	35 ± 6
$\sigma_{ep \to J/\psi\ ep}$(nb)	$7.4 \pm 1.2 \pm 1.6$	$6.7 \pm 1.2 \pm 2.0$

channel	e^+e^-	
$W_{\gamma^* p}$ range (GeV)	40-75	75-140
acceptance	26.8%	22.8%
signal events	32 ± 7	24 ± 6
$\sigma_{ep \to J/\psi\ ep}$(nb)	$3.8 \pm 0.8 \pm 0.8$	$3.4 \pm 0.8 \pm 0.7$
Int. photon flux	0.061	0.049
$\sigma_{\gamma p \to J/\psi\ p}$(nb)	$62 \pm 13 \pm 13$	$70 \pm 16 \pm 13$

channel	$\mu^+\mu^-$	
$W_{\gamma^* p}$ range (GeV)	40-90	90-140
acceptance	14.9%	23.4%
signal events	16 ± 4	19 ± 5
$\sigma_{ep \to J/\psi\ ep}$(nb)	$3.7 \pm 0.9 \pm 1.1$	$2.8 \pm 0.7 \pm 0.8$
Int. photon flux	0.077	0.033
$\sigma_{\gamma p \to J/\psi\ p}$(nb)	$48 \pm 12 \pm 14$	$84 \pm 21 \pm 24$

Table 1. Cross section for ep $\to$ e J/ψ p and γp $\to$ J/ψ p

6. Summary

A sample of $\approx$ 74 events containing D*(2010) was isolated in ep collisions at HERA using the ZEUS detector. The preliminary cross section for the kinematic region { $p_T(D^*) \geq 1.7$ GeV , $|\eta(D^*)| < 1.5$ } was found to be $1.5 \pm 0.3(stat) \pm 0.3(syst)$ nb. Extrapolation outside the selected kinematic range, gave a total charm cross section of $\sigma(ep \to c\bar{c}X) \sim 1.7\,\mu$b assuming MRSD-/LAC1 and $\sim 1\,\mu$b for MRSD-/GRV. The sensitivity in the present analysis to the proton and photon structure functions is limited due to the requirement of $|\eta(D^*)| < 1.5$.

The results of a preliminary measurement of ep$\to$ eJ/ψp cross section for $Q^2 \leq$ 3 GeV^2 and 40 $\leq$ $W_{\gamma^* p}$ $\leq$ 140 GeV are $7.4 \pm 1.2 \pm 1.6$nb^{-1} for the electron channel and $6.7 \pm 1.2 \pm 2.0$nb^{-1} for the muon channel, respectively. It should be noted that a fraction of the events where the proton diffractively dissociates could be contained in the final data sample.

References

[1] Review of Particle Properties, Phys. Rev. **D50** (1994) .

[2] ZEUS Collab., The ZEUS Detector, Status Report, DESY (1993).
ZEUS Collab., M. Derrick et al., Phys. Lett. **B293** (1992) 465.

[3] G. Marchesini et al., Computer Phys. Comm. **67** (1992) 465.
B.R. Webber, HERWIG at HERA DESY 92-028, Proc. of the Workshop "Physics at HERA", Vol III., Oct 1991, p. 1354.
L. Stanco, ibidem, p. 1363.

[4] T. Sjoestrand, Zeit. Phys. **C42** (1989) 301 and in Proc. of the Workshop on Physics at HERA, DESY Vol III (1992) 1405.

[5] M. Ryskin, Zeit. Phys. **C57** (1993) 89.

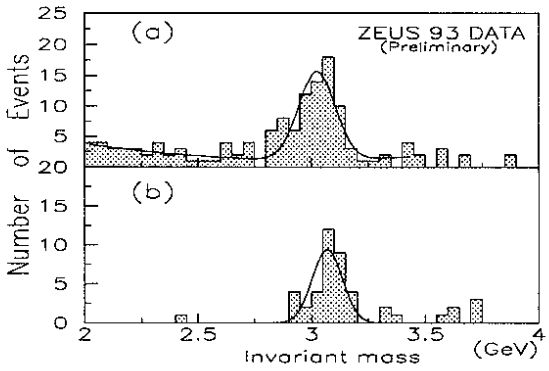

Figure 3. Invariant mass of J/ψ candidates. (a) e^+e^- and (b) $\mu^+\mu^-$ mode. The superimposed curves are (a) a Gaussian and a second order polynomial, and (b) a Gaussian.

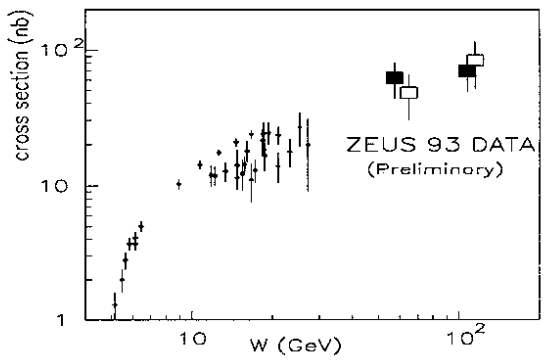

Figure 4. A compilation of $\sigma(\gamma p)$ values as a function of $W_{\gamma^* p}$ for $\gamma p \to \psi N, \gamma p \to \psi p$. The squares show the results of the present paper. Solid squares are for the e^+e^- and open squares for the $\mu^+\mu^-$ mode.

[6] H. Jung, DESY 92-028, and in Proc. of the Workshop "Physics at HERA", Vol III., Oct 1991, p. 1488.

[7] F. Butler et al., (CLEO Collaboration), Phys. Rev. Lett. **69** (1992) 2041;
D.S. Akerib et al., (CLEO Collaboration), Phys. Rev. Lett. **71** (1993) 3070;
H. Albrecht et al., (ARGUS Collaboration), DESY 94-094 preprint.

[8] A.D. Martin, R.G. Roberts and W.J. Stirling, Phys. Rev. **D47** (1993) 867.

[9] H. Abramowicz, K. Charchula and A. Levy, Phys. Lett. **B269** (1991) 458.

[10] M. Glück,E. Reya and A. Vogt, Phys. Rev. **D46** (1992) 1973.

[11] P. Aurenche et al., Zeit. Phys. **C56** (1992) 589.

[12] M. Drees and K. Grassie, Zeit. Phys. **C28** (1985) 451.

[13] V.N. Gribov, V.A. Kolkunov, L.B. Okun, V.M. Shekhter, Sov. Phys. JEPT **14** (1962) 1308.
B. Burow, Ph.D. Thesis, Graduate Dept. of Physics, University of Toronto, Canada (1994) available as Internal Report DESY F35D-94-01 February 1994.

[14] A. Baldini et.al., Landolt-Bornstein, Group I, Vol 12b, Springer-Verlag, ed. H.Schopper.
S. Holmes, W. Lee & J. Wiss, Ann. Rev. Nucl. Part. Sci. **35** (1985) 397.

Multi-Jet Production and a Determination of α_s

S Söldner–Rembold

Albert-Ludwigs-Universität Freiburg, Fakultät für Physik, 79104 Freiburg im Breisgau, Germany

On behalf of the ZEUS and H1 Collaborations

Abstract

Multi-jet production in deep-inelastic electron-proton scattering (DIS) has been studied at HERA using the JADE algorithm. The ZEUS collaboration has compared the partonic scaling variables and the rate of two jet production to perturbative $\mathcal{O}(\alpha_s^2)$ QCD calculations. The H1 collaboration has observed the running of α_s as a function of Q^2. A preliminary measurement yields $\alpha_s(M_Z) = 0.121 \pm 0.009(\text{stat.}) \pm 0.012(\text{syst.})$.

1. Introduction

Deep-inelastic neutral current ep scattering without QCD corrections leads to a 1+1 parton configuration in the final state, where "+1" denotes the proton remnant. At leading order, $\mathcal{O}(\alpha_s)$, QCD processes contribute significantly to the ep cross section at HERA energies: Boson-Gluon-Fusion, where the virtual boson interacts with a $q\bar{q}$ pair originating from a gluon in the proton, and QCD-Compton scattering, where a gluon is radiated by the scattered quark. Both processes lead to a two ($\hat{=}$2+1) jet topology.

On the partonic level, the kinematics and the rate R_{2+1} of two jet production can be described by perturbative QCD calculations with only one free parameter, the strong coupling constant α_s. HERA has the unique opportunity to study the running of α_s over a wide range in Q^2 ($10 < Q^2 < 10^4$ GeV^2) from the Q^2 dependence of the 2+1 jet production rate.

A determination of $\alpha_s(Q^2)$ requires detailed understanding of the jet kinematics. The ZEUS collaboration has therefore compared the measurement of the underlying parton dynamics and the jet rates to next-to-leading order (NLO or $\mathcal{O}(\alpha_s^2)$) calculations. The H1 collaboration has determined the value of $\alpha_s(M_Z)$. In addition, first evidence is presented for the running of α_s from DIS at HERA.

2. Monte Carlo simulations

The LEPTO 6.1 Monte Carlo event generator contains the exact $\mathcal{O}(\alpha_s)$ matrix element (ME) and the parton shower (PS) in the leading log approximation [1]. In order to simulate at the same time the hard emission of partons and the higher order parton shower, a combined option (MEPS) exists which is used to describe the HERA data for the correction of experimental inefficiencies.

3. Theoretical calculations

The Monte Carlo program does not include the exact NLO matrix element calculation. However, the NLO corrections to the 2+1 jet cross section due to irresolvable 3+1 jet events and due to virtual corrections are significant [2]. They are taken into account in the program DISJET of T. Brodkorb and E. Mirkes [3]. A similiar program by D. Graudenz called PROJET [4] is available, but it does not include the NLO corrections to the longitudinal part of the cross section.

4. Jet finding

Both HERA experiments have used the JADE algorithm [5] to relate partons to observable jets. The scaled

invariant mass of two massless objects (partons or calorimeter cells) i and j is given by

$$y_{ij} = \frac{2E_iE_j(1-\cos\theta_{ij})}{W^2}. \quad (1)$$

The minimum y_{ij} of all possible combinations is found. If the value of this minimum y_{ij} is less than the cut-off parameter y_{cut}, the two objects i and j are merged by adding their four-momenta and the process is repeated until all $y_{ij} > y_{cut}$.

In the data, a fictitious cluster (called pseudo-particle) in the forward (z) direction is added to which the missing longitudinal momentum for each event is assigned. The pseudo-particle is treated like any other particle in the JADE scheme. The pseudo-particle procedure together with the choice of the visible hadronic invariant mass W_{vis} as jet scale minimizes detector corrections. W_{vis} is calculated from just those calorimeter cells associated with the hadrons.

The JADE algorithm has been used here since it is currently the only algorithm which allows comparison to $\mathcal{O}(\alpha_s^2)$ calculations. However, it has been shown previously that the performance of the JADE algorithm in reconstructing jets is worse than for other algorithms [6].

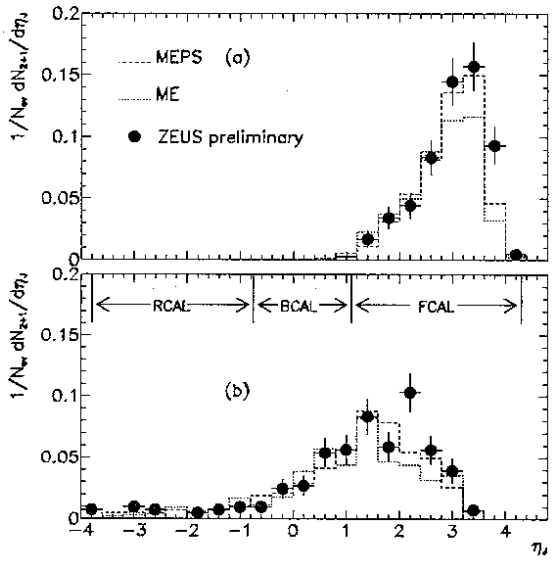

Figure 1. Pseudorapidity η_j of the two jets: **(a)** higher η jet; **(b)** lower η jet. Uncorrected data are compared to the MEPS and the ME simulations. The acceptance ranges of the different sections of the ZEUS calorimeter are indicated.

5. Data sets

The H1 event sample is defined by $W^2 > 5000$ GeV^2, an identified scattered electron with $E_{e'} > 14$ GeV, $160° < \theta_{e'} < 172.5°$ and $10 < Q^2_{e'} < 100$ GeV^2 in the backward calorimeter, or with $y_{e'} < 0.7$, $\theta_{e'} < 148°$ and $Q^2_{e'} > 100$ GeV^2 in the central calorimeter.

ZEUS has limited the kinematic range for the jet analysis to $160 < Q^2 < 1280$ GeV, $0.01 < x < 0.1$ and $0.04 < y < 0.95$. At high Q^2, jet structures should be more pronounced and hadronization uncertainties are minimized. At high x, the phase space for jet production increases and the systematic error from the structure function dependence of the jet rate is reduced.

The data corresponds to a luminosity of 0.24 pb^{-1} (H1) and 0.55 pb^{-1} (ZEUS).

6. Two jet properties

In Fig. 1, the jets are ordered in pseudorapidity $\eta_j = -\ln\tan(\theta_j/2)$. The higher η jet is usually found very close to the forward beam pipe. Fig. 1a shows that the prediction of the η_j distribution by the ME and the MEPS Monte Carlo models describe the data fairly well apart from the very forward region $\eta_j > 3.6$, where the predictions are significantly below the data. In this region the results depend on the description of the initial state parton shower and the target fragmentation in the Monte Carlo generator as well as on the simulation of the response of the calorimeter around the forward beam pipe.

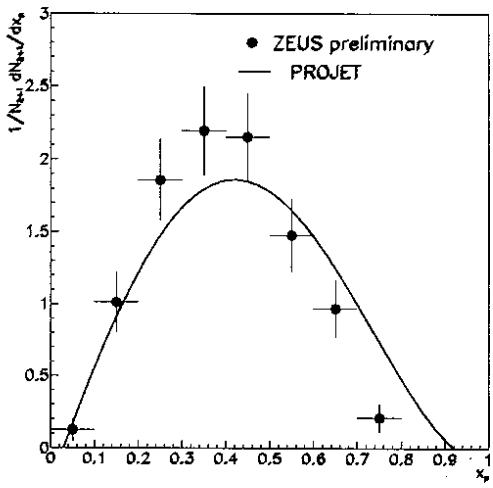

Figure 2. Uncorrected x_p distribution compared to a $\mathcal{O}(\alpha_s^2)$ QCD calculation (PROJET).

The cross section for 2+1 jet production is obtained by integrating over the partonic scaling variables $x_p = Q^2/(2q\cdot p_p) = x/\xi$ and $z_p = (P\cdot p_p)/(P\cdot q)$ [7]. The momentum p_p of the incoming parton is given by the fraction ξ of the proton momentum P, $p_p = \xi P$. Experimentally, x_p is calculated from the invariant mass $M^2_{JJ} = y_{cut}W^2$ of the two jet system using

$$x_p = \frac{Q^2}{Q^2 + M^2_{JJ}}.$$

z_p is measured from the relative contribution to $(E-p_z)$ of the partons or cells assigned to the jet in the lab,

$$z_p = \frac{\sum_{jet}(E-p_z)}{\sum_{hadrons}(E-p_z)}.$$

The uncorrected x_p distribution is compared to the PROJET calculation in Fig. 2. The mean of the distribution lies at $\langle x_p \rangle \approx 0.5$ ($Q^2 \approx M_{JJ}^2$), i. e. the two jet system has a large invariant mass ($\langle M_{JJ} \rangle \approx 23$ GeV). The singularity in the 2+1 cross section at $x_p \to 1$ is cut off by the y_{cut} parameter.

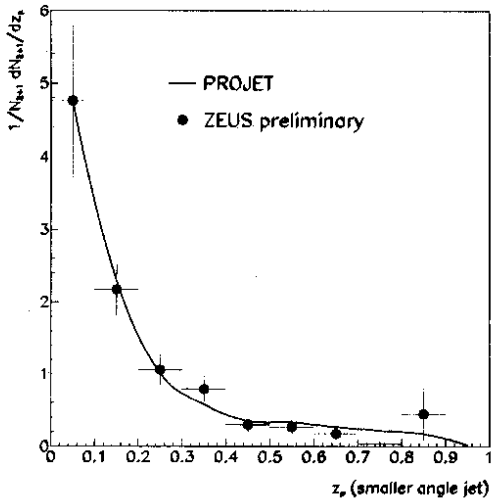

Figure 3. z_p distribution compared to a $\mathcal{O}(\alpha_s^2)$ QCD calculation (PROJET). The correction to the parton level is done using the ME model.

Only the z_p distribution for the smaller angle jet is shown in Fig. 3, since $z_p^{(1)} + z_p^{(2)} \approx 1$ and $z_p^{remnant} \approx 0$. The z_p distribution is well described by the PROJET calculation. The cross section rises strongly at $z_p \to 0$, because of the small influence of y_{cut} on the cut-off of the z_p singularity in the JADE algorithm. This leads to the forward peak in the jet angular distribution in the lab.

The transverse momentum P_T of the jets in the γ^*-parton CMS is given in LO by $P_T^2 = Q^2 z_p(1-x_p)(1-z_p)/x_p$. The average transverse momentum $\langle P_T \rangle$ of the jets in the γ^*-parton CMS is about 10 GeV (Fig. 4) and the minimum P_T is about 3 GeV. This is sufficiently large to ensure the validity of a perturbative QCD calculation. The distribution is well described by the two Monte Carlo models.

7. Jet rates and the determination of α_s

ZEUS has defined the 2+1 jet rate R_{2+1} by the ratio of the number of events

$$R_{2+1} = \frac{N_{2+1}}{N_{2+1} + N_{1+1}}.$$

This definition reduces the dependence on the 3+1 jet rate, which is only calculated at the tree level in PROJET and DISJET. Experimentally, the acceptance correction factors for the 3+1 jet rate are large.

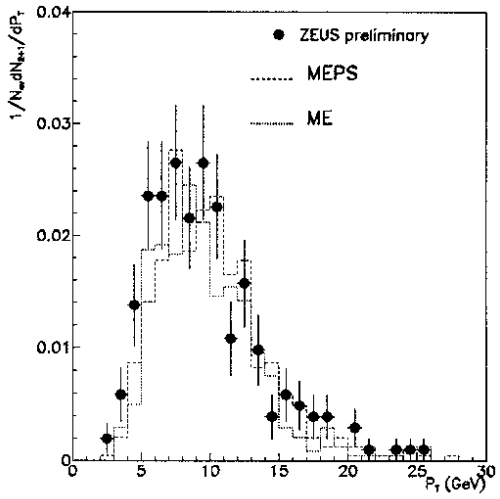

Figure 4. The transverse momentum P_T of one of the two jets in the γ^*-parton center of mass system. The uncorrected data are compared to the MEPS and the ME simulations.

In Fig. 5, the corrected jet production rates are shown as a function of the jet resolution parameter y_{cut}. The correction to the parton level is done using the MEPS model. The 2+1 jet rate increases with finer jet resolution (smaller y_{cut}).

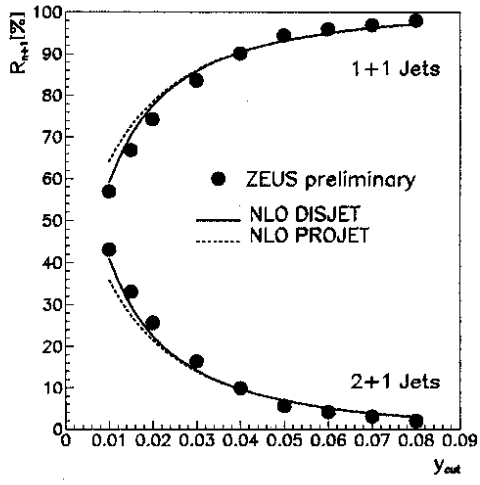

Figure 5. The corrected jet production rate R_{n+1} in % as a function of y_{cut} is compared to the NLO calculation of the programs PROJET [4] and DISJET [3] at the parton level. Only statistical errors are shown.

For comparison the NLO calculations of the programs DISJET [3] and PROJET [4] are also shown. The difference between them is due to the missing NLO corrections to the longitudinal cross section.

The errors shown are the statistical binomial errors which are highly correlated, because all 2+1 jet events

at a given y_{cut} are included in the points at smaller y_{cut}. These correlations are avoided by redefining the data in terms of the differential jet rate

$$D_{1+1}(y_{cut}) = \frac{R_{1+1}(y_{cut}) - R_{1+1}(y_{cut} - \Delta y_{cut})}{\Delta y_{cut}},$$

where every event enters only once. In Fig. 6 the differential jet rate D_{1+1} is shown together with the statistical errors and the DISJET calculation.

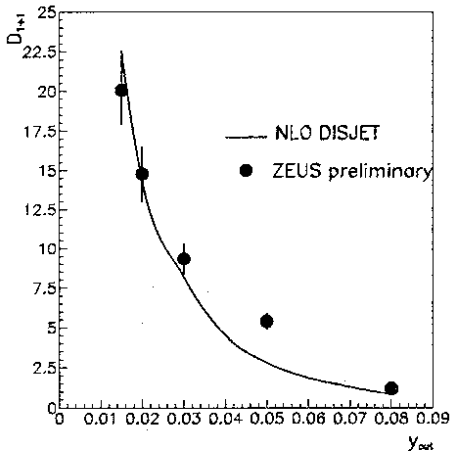

Figure 6. The differential jet rate D_{1+1} calculated from the corrected jet rate R_{1+1} (Fig. 5) as a function of y_{cut}. D_{1+1} is compared to the NLO calculation of the program DISJET [3].

Comparing Fig. 6 with the jet production rates R_{n+1} shows that the apparent systematic deviations from the QCD models above and below $y_{cut} = 0.04$ in Fig. 5 are caused by the correlation between the points. The differential jet rate D_{1+1} is well described by the NLO QCD calculations, apart from a deviation at $y_{cut} = 0.05$.

The QCD calculations contain α_s as the only free parameter. For the comparisons in Figs. 5 and 6, a value of $\Lambda^{(5)}_{\overline{MS}} = 312$ MeV was chosen which corresponds to $\alpha_s(M_Z^2) = 0.124$. This is a value measured from jet rates in e^+e^- annihilations [8].

H1 has extracted α_s from the $R_{2+1} = \sigma_{2+1}/\sigma_{tot}$ measurement in different Q^2 ranges by fitting it to the jet rate at $y_{cut} = 0.02$ using the PROJET calculation (Fig. 7a).

The jet angles θ_j have to be inside the range $10^\circ < \theta_j < 160^\circ$ which reduces the dependence on the description of the very forward region. In order to minimize the systematic error due to the parametrization of the parton densities, an additional cut $\xi > 0.01$ was introduced. The parton densities affect R_{2+1} mainly through the 1+1 jet cross section at low x [2]. For 1+1 jet events, $\xi = x > 0.01$, and for 2+1 jet events the cut is trivially fullfilled because $\xi > y_{cut} = 0.02$.

The running of $\alpha_s(Q^2)$ is preferred by the data in Fig. 7b, where the curves represent $\alpha_s(Q^2) = \text{const.}$

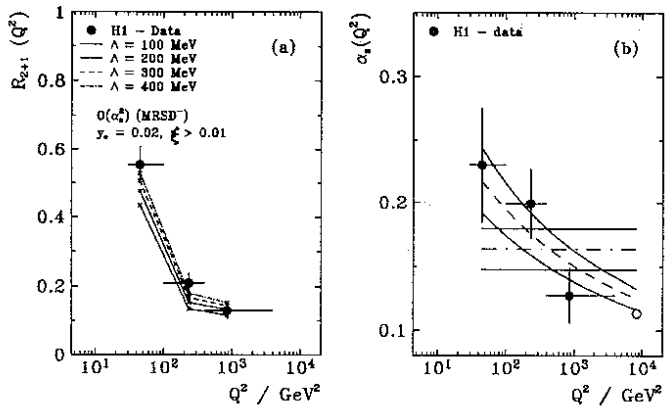

Figure 7. a) R_{2+1} versus Q^2 at $y_{cut} = 0.02$ and $\xi > 0.01$. PROJET calculations with different values of $\Lambda^{(4)}_{\overline{MS}}$ and the MRSD$^-$ structure function are superimposed. b) α_s versus Q^2. The curves represent $\alpha_s(Q^2) = \text{const.}$ and a running $\alpha_s(Q^2)$ with $\alpha_s(M_Z) = 0.121$. The open circle is the world average $\alpha_s(M_Z) = 0.118$.

and an $\mathcal{O}(\alpha_s^2)$ calculation of the Q^2 dependence. An extrapolation yields $\alpha_s(M_Z) = 0.121 \pm 0.009(\text{stat.}) \pm 0.012(\text{syst.})$, where the preliminary systematic error includes the y_{cut} dependence (± 0.003), the uncertainties due to the hadronic energy scale of the calorimeter ($\pm^{0.006}_{0.007}$), the parton densities (± 0.005) and the renormalization scale (± 0.006). At low Q^2 the model dependence of the hadronization correction is another important source of systematic errors.

8. Conclusions

Jet production in DIS at high Q^2 is well described by perturbative $\mathcal{O}(\alpha_s^2)$ QCD calculations. First evidence from HERA for the running of α_s has been presented and a preliminary H1 measurement yields $\alpha_s(M_Z) = 0.121 \pm 0.009(\text{stat.}) \pm 0.012(\text{syst.})$.

References

[1] G. Ingelman, Proc. of the Workshop on Physics at HERA 1991, Vol 3 p. 1366; Eds. W. Buchmüller and G. Ingelman (DESY, Hamburg, 1992); M. Bengtsson, G. Ingelman and T. Sjöstrand, Nucl. Phys. **B301** (1988) 554.

[2] D. Graudenz, Phys. Lett. **B256** (1991) 518.

[3] T. Brodkorb, E. Mirkes, University of Wisconsin Preprint: MAD-PH-821 (April 1994).

[4] D. Graudenz, PROJET 3.6, to be published.

[5] JADE Collaboration: W. Bartel *et al.*, Z. Phys. **C33** (1986) 23; JADE Collaboration: S. Bethke *et al.*, Phys. Lett. **B213** (1988) 235.

[6] V. Hedberg *et al.*, DESY preprint: DESY 93-190 (1993).

[7] K. H. Streng, T. F. Walsh, P. M. Zerwas, Z. Phys. **C2** (1979) 237.

[8] S. Bethke, Lectures given at the Scottish Universities Summer School, St. Andrews, Scotland, August 1–21, 1993, Heidelberg preprint: HD-PY 93/7.

Search for Leptoquarks in ep collisions at $\sqrt{s} = 296$ GeV

Bruce Straub

Columbia University
New York, NY 10027

ZEUS Collaboration

Abstract

Using the ZEUS detector at HERA, we have searched for leptoquarks decaying into eq, νq, μq, or τq in a data sample of 0.55 pb^{-1}. No leptoquark signal was observed. Limits on coupling *vs.* mass were determined for the various leptoquark types. For electroweak coupling strength, scalar leptoquarks which decay to eq with masses below 242 GeV were excluded at 95% confidence.

1. Introduction

Leptoquarks (LQs) are color-triplet bosons with both lepton and baryon number. In ep collisions, a LQ would be produced as an s-channel resonance via electron-quark fusion. Using the ZEUS detector[1] at HERA, in a data sample of 0.55 pb^{-1}, we have searched for LQs which decay to eq, νq, μq, and τq in collisions of 26.7 GeV electrons with 820 GeV protons.

LQs decaying into eq or νq, called first-generation LQs, would have an event topology identical to neutral or charged current deep-inelastic scattering (DIS) events respectively. The signal for a LQ would be a peak at M_{LQ}^2/s in the DIS x-distribution (M_{LQ} is the leptoquark mass). LQs decaying into eq can also be distinguished from neutral-current DIS by their distribution in $y = Q^2/xs$. At fixed x, the neutral-current DIS cross section behaves roughly as y^{-2}, so this background can be supressed by a cut of the form $y > y_{min}$. In $LQ \rightarrow eq$, y is related to θ^*, the LQ-rest-frame angle between the incident and final-state electrons, by $y = (1 - \cos\theta^*)/2$. Scalar LQs would have a flat y distribution, while vector LQs would have a $(1-y)^2$ distribution.

We have set coupling *vs.* mass limits for all $SU(3) \times SU(2) \times U(1)$ invariant first-generation LQs which conserve baryon and lepton number[2]. In the narrow-width approximation, the production cross section is:

$$\sigma_{ep\rightarrow LQ} = \frac{\pi}{4s}\left(g_R^2 + g_L^2\right) q\left(M_{LQ}^2/s\right) \begin{cases} \times 1 & \text{scalar} \\ \times 2 & \text{vector} \end{cases}$$

where g_L and g_R are the left and right-handed couplings and $q(x)$ is the quark density to which the LQ couples.

There exist limits on LQ couplings from low-energy experiments[3, 4, 5]. An important one is derived from the agreement between standard-model calculations and measurements of the $\pi \rightarrow e\nu_e$ decay rate. Because of the resulting severe limit, $g_L g_R < (M_{LQ}/8.8\ \text{Tev})^4$, we consider only first-generation LQs for which either g_L or g_R vanish.

A LQ formed in eq could also couple to μ or τ leptons[6]. Stringent limits[3, 4] on $\mu A \rightarrow e + X$ effectively rule out LQs coupling to both eq and $\mu q'$, if q and q' are both light quarks. If, however, q' is a heavy quark, then such LQs could exist with relatively large couplings ($g \sim 0.1$), as could LQs coupling to eq and $\tau q'$ (even if q' is light).

2. Simulation of signals and backgrounds

The backgrounds considered were: neutral and charged-current DIS, simulated using `Lepto`[7], `Heracles`[8] and `Ariadne`[9], and direct and resolved photoproduction (γp) processes, generated using `Herwig`[10]. γp events

can be backgrounds for $LQ \rightarrow eq$ if a fake electron is found. The structure function parameterizations used were MRSD0[11] for the proton, and GRVG0[12] for the photon. `Pythia`[13] was used to simulate scalar LQs decaying to eq, νq, μc, and τb. We searched for LQs with masses between 60 GeV and 260 GeV and generated Monte Carlo samples at 20 GeV intervals in this region. To simulate vector LQs, the samples were reweighted according to the generated y.

3. Data selection and reconstruction

We use a coordinate system in which beam protons travel in the $+z$ direction for which the polar angle, θ, is zero. This analysis relied mainly on the uranium-scintillator calorimeter[14], the central tracking detector (CTD)[15], and the vertex detector (VXD)[16]. The calorimeter has three parts: Forward ($1.6° < \theta < 36.8°$), Barrel ($36.8° < \theta < 129.4°$), and Rear ($129.4° < \theta < 177.4°$). The acceptance of the CTD covers $13° < \theta < 167°$, and the VXD covers $9° < \theta < 165°$.

Separate event selections were made for eq and νq final states. The μq and τq searches were performed by making additional cuts on the νq sample. Cuts common to both samples were: the requirement that an acceptable vertex was reconstructed in the CTD and the VXD, the rejection of events with more than 5 GeV in the electron calorimeter of the luminosity monitor (to reduce γp background), calorimeter timing cuts (to reject beam-gas and cosmic rays), and rejection of beam-halo muons and cosmic rays using pattern recognition.

Events in the $LQ \rightarrow eq$ sample were required to have an isolated electron with energy above 10 GeV and a matching CTD track. $E - P_z$ was required to be between 35 GeV and 65 GeV (E is the total energy measured in the calorimeter, P_z the total z-momentum). To reduce low-Q^2 backgrounds, the transverse energy (E_t) had to exceed 20 GeV and the energy with $\theta > 150°$ had to be less than 5 GeV. A total of 1330 events passed these cuts. The (M_{LQ} dependent) efficiency of the trigger and offline cuts for $LQ \rightarrow eq$ was between 74% and 82% for scalar LQs. Using triggers in unpaired e^- and p bunches, we estimate the non-ep contamination of this sample to be well below 1%. We used the double-angle (DA) method to reconstruct x and y for the eq sample. Figure 1 shows the distribution of x_{DA} for the entire eq sample and for $Q^2_{DA} > 500$ GeV^2. No LQ signal is seen.

The $LQ \rightarrow \nu q$ selection required that the net transverse momentum measured in the calorimeter ($\not\!\!P_t$) exceed 10 GeV and that $E - P_z < 55$ GeV. Of the 48 events passing these cuts, 15 were rejected because an isolated electron of than 10 GeV was found. Three more non-ep triggers were rejected by scanning. A final cut (to reject γp events with mismeasured $\not\!\!P_t$) required

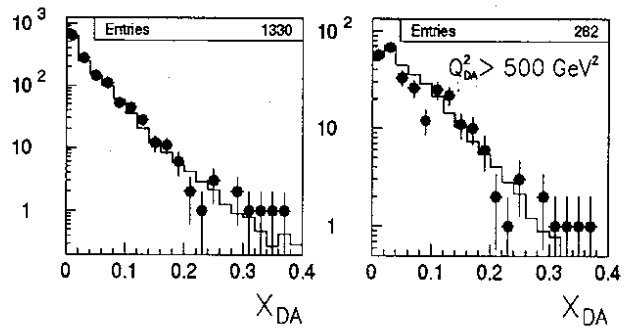

Figure 1. The dots are the number of events *vs.* x_{DA} for the entire eq sample, and for those events with $Q^2_{DA} > 500\text{GeV}^2$. The histograms are neutral current DIS Monte Carlo.

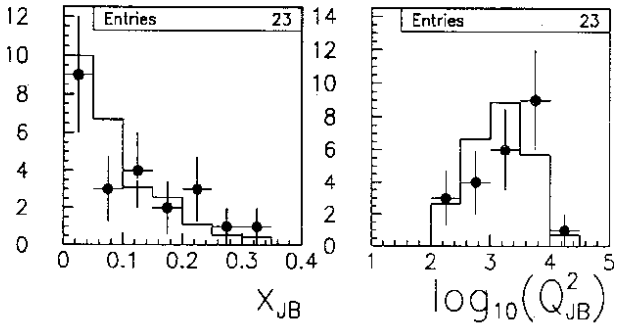

Figure 2. Distributions of x_{JB} and Q^2_{JB} (GeV^2) for the νq sample (dots) and charged-current DIS Monte Carlo (histograms).

that $\not\!\!P_t/E_t > 0.4$, leaving 23 events, consistent with the charged-current DIS Monte Carlo estimation of 24.6 events. The M_{LQ} dependent efficiency of the trigger and offline cuts for scalar LQs decaying into νq was above 76%. We used the Jacquet-Blondell (JB) method to reconstruct x and y for the νq events. Figure 2 shows x_{JB} and Q^2_{JB} distributions for the selected events and for charged-current DIS Monte Carlo. The measured distributions agree well with the Monte Carlo expectation.

The μq candidates were selected using only the calorimeter and the CTD. Because high-energy muons typically deposit only a few GeV in the calorimeter, we could base our search for $LQ \rightarrow \mu q$ on the νq sample (for which $\not\!\!P_t > 10$ GeV). We required an isolated calorimeter cluster which was compatible with being a minimum ionizing particle, had a matching CTD track, and was within 15° in azimuth of the $\not\!\!P_t$ vector. To preserve efficiency for high-mass LQs, where the muon polar is often too small to be in the CTD acceptance, we also accepted any νq candidate with $\not\!\!P_t > 80$ GeV. No events passed the μq cuts. The estimated background

from DIS and γp was 0.46 events. The overall efficiency of the μq cuts for scalar and vector LQs decaying into μc is above 60% over the M_{LQ} range.

Significant $\not{P}_t$ is also expected in τq LQ decays. We based the τq search on the νq sample before the isolated-electron rejection was applied (48 events). Separate selections were made for each τ decay mode. For $\tau \to e\nu_\tau\overline{\nu}_e$, we required $\not{P}_t > 15$ GeV and an isolated electron with energy above 10 GeV. For $\tau \to \mu\nu_\tau\overline{\nu}_\mu$, all events in the μq sample were accepted. Finally, for $\tau \to \nu_\tau +$ hadrons, we required $E_t > 40$ GeV (to reduce γp) and $\not{P}_t/E_t < 0.7$ (to reject charged-current DIS). Also, an isolated, compact ($R_{\eta\phi} < 0.3$) calorimeter cluster with energy above 10 GeV had to be found with $\theta > 10.4°$, $P_t > 5$ GeV, and 1, 2, or 3 matching CTD tracks. Here also, we accepted any νq event with $\not{P}_t > 80$ GeV. No events passed the τq cuts for any of the three modes. The estimated background from DIS and γp was 0.68 events. The efficiency of the cuts exceeded 40% for scalar (vector) LQs with $M_{LQ} > 110$ GeV ($M_{LQ} > 160$ GeV).

4. Procedure for calculating limits

To determine coupling limits *vs.* M_{LQ} for first-generation LQs, we applied M_{LQ} dependent cuts to the eq and νq samples. For the eq events, the cut $x_{min}(M_{LQ}) < x_{DA} < x_{max}(M_{LQ})$ selected events within the x peak region. The additional cut $y_{DA} > y_{min}(M_{LQ})$ was applied to suppress neutral-current DIS. For the νq sample, only an x cut was applied: $x_{min}(M_{LQ}) < x_{JB} < x_{max}(M_{LQ})$.

Using the Monte Carlo samples, we determined the values of x_{min}, x_{max} (and y_{min} for eq decays), for which, in the absence of a signal, the *average cross-section limit* would be minimized. These cut parameters were fit to a polynomial in M_{LQ}, as were the resulting signal efficiencies and expected background.

We took uncertainties in the luminosity (3.3%), the background estimation (10%), and the signal efficiency(2%) into account by treating these quantities as Gaussian random variables and setting the LQ cross-section limits to the value for which, in repeated experiments, we would have observed more events than we did with 95% probability. The effect of these uncertainties is to increase the cross-section limits by at most 4%.

5. Coupling Limits

The coupling limit *vs.* M_{LQ} curves for scalar LQs are shown in figure 3 and for vector LQs in figure 4 (all limits are at 95% confidence level). The coupling and state names follow the conventions of reference [2]. For fermion number (F) equal to -2, scalar and vector LQs

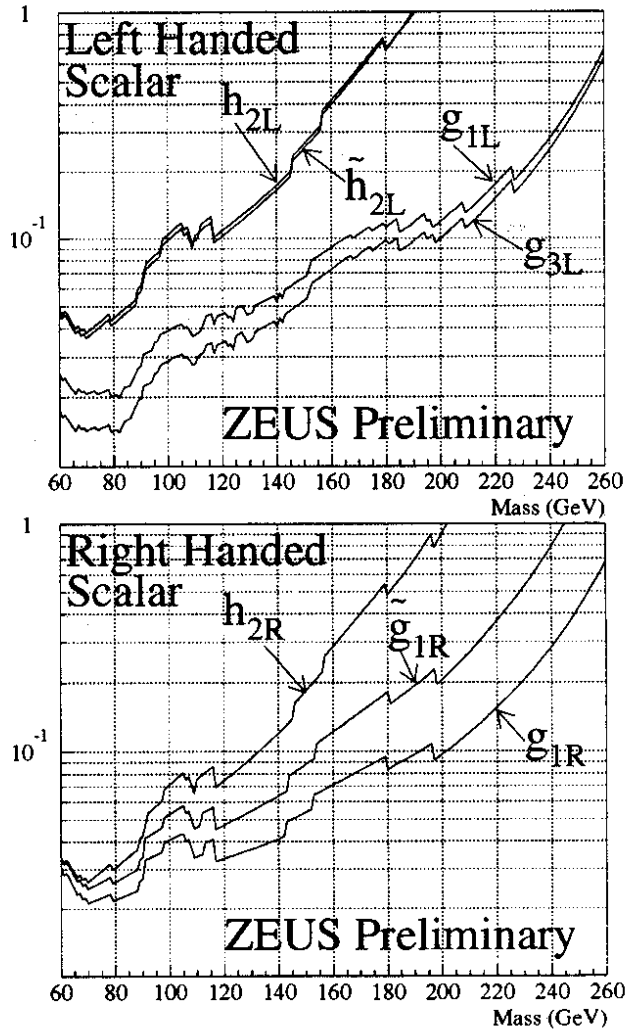

Figure 3. The 95% confidence level limits on couplings for first-generation scalar leptoquarks.

and the couplings are labeled S, V, and g respectively (for $F = 0$, R, U, and h are used). The subscripts give the dimension of the $SU(2)$ representation. Since the e^-q initial state has $F = -2$, much stronger limits are set on those couplings. Table 1 summarizes the mass limits for coupling strengths of $g = 0.1$ and $g = (4\pi\alpha_{EW})^{1/2} = 0.31$.

For flavor-violating LQs we set limits on $g\mathcal{B}$ where g is the coupling to eq at the production vertex and $\mathcal{B}$ is the branching fraction into the final state. For $LQ \to \mu c$ we set limits on $g_{eu}\mathcal{B}_{\mu c}$ as shown in figure 5. For g_{eu} with electroweak strength and a branching fraction $\mathcal{B}_{\mu c}$ of 50%, we have excluded S_1 LQs with $M_{LQ} < 238$ GeV and $\tilde{V}_2$ LQs with $M_{LQ} < 246$ GeV. Also shown in figure 5 are limits on $g_{ed}\mathcal{B}_{\tau b}$. Again assuming electroweak coupling for g_{ed} and $\mathcal{B}_{\tau b} = 50\%$, we have excluded $\tilde{S}_1$ LQs with $M_{LQ} < 207$ GeV, and V_2 LQs with $M_{LQ} < 216$ GeV.

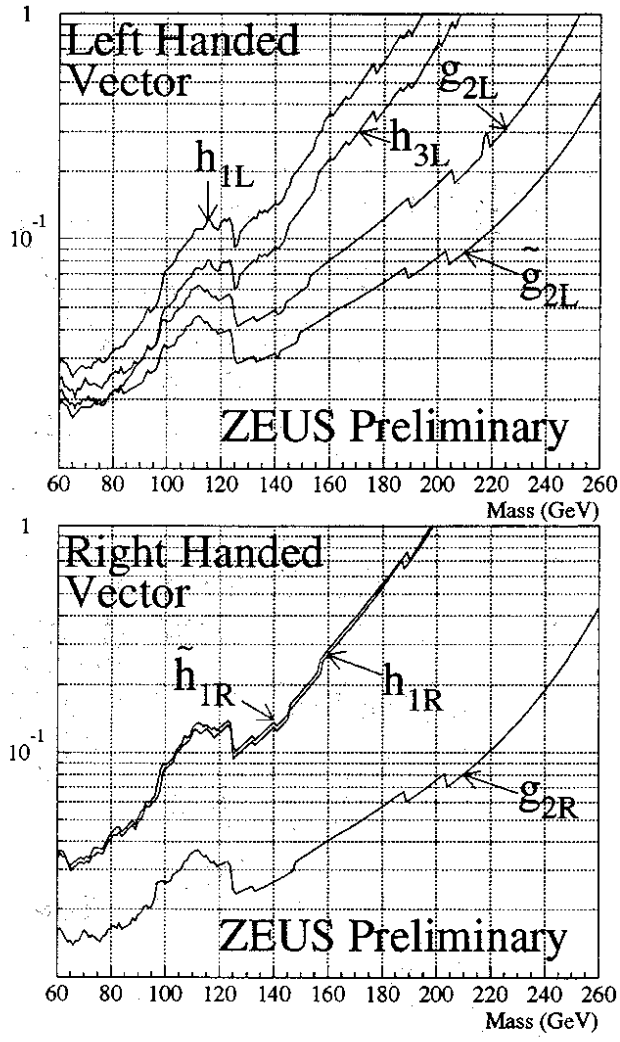

Figure 4. The 95% confidence level limits on couplings for first-generation vector leptoquarks.

coupling/ state		Q	$\mathcal{B}_{\nu q}$	M_{LQ} limit $g = 0.1$	M_{LQ} limit $g^2 = 4\pi\alpha_{EW}$
g_{1L}	S_1	$-1/3$	1/2	164 GeV	242 GeV
g_{3L}	S_3	$-4/3, -1/3$	0, 1/2	183 GeV	245 GeV
h_{2L}	R_2	$-5/3$	0	98 GeV	155 GeV
$\tilde{h}_{2L}$	$\tilde{R}_2$	$-2/3$	0	100 GeV	156 GeV
g_{1R}	$\tilde{S}_1$	$-1/3$	0	191 GeV	242 GeV
$\tilde{g}_{1R}$	$\tilde{S}_1$	$-4/3$	0	153 GeV	214 GeV
h_{2R}	R_2	$-5/3, -2/3$	0, 0	132 GeV	162 GeV
g_{2L}	V_2	$-4/3$	0	170 GeV	224 GeV
$\tilde{g}_{2L}$	$\tilde{V}_2$	$-1/3$	0	215 GeV	251 GeV
h_{1L}	U_1	$-2/3$	1/2	108 GeV	157 GeV
h_{3L}	U_3	$-5/3, -2/3$	0, 1/2	143 GeV	171 GeV
g_{2R}	V_2	$-4/3, -1/3$	0, 0	219 GeV	252 GeV
h_{1R}	U_1	$-2/3$	0	104 GeV	164 GeV
$\tilde{h}_{1R}$	$\tilde{U}_1$	$-5/3$	0	103 GeV	162 GeV

Table 1. First-generation LQ mass limits for couplings $g = 0.1$ and $g^2 = 4\pi\alpha_{EW}$. The columns labeled Q and $\mathcal{B}_{\nu q}$ give the charge and the branching ratio into νq for those members of $SU(2)$ multiplet which can be produced in $e^- p$ collisions. The nomenclature is taken from reference [2]

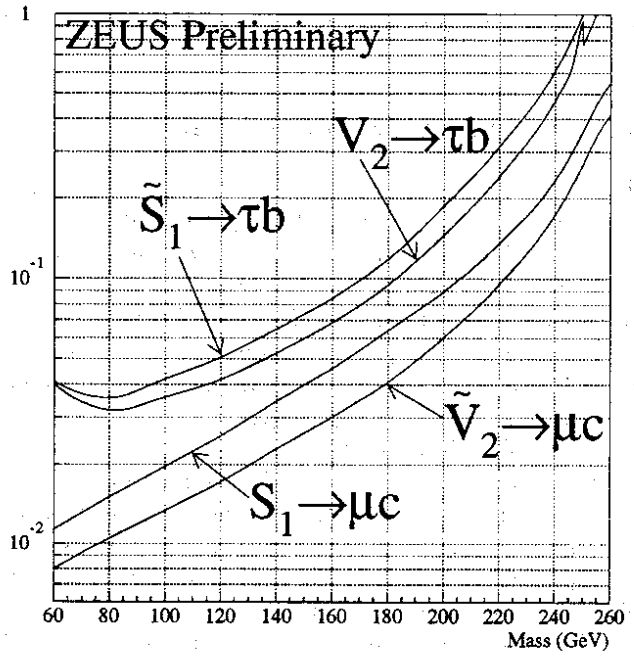

Figure 5. The two lower curves are the 95% confidence level limits on $g_{eu}\mathcal{B}^{1/2}_{\mu c}$ for S_1 and $\tilde{V}_2$ LQs. The two upper curves give the limits on $g_{ed}\mathcal{B}^{1/2}_{\tau b}$ for $\tilde{S}_1$ and V_2 LQs.

References

[1] The ZEUS Detector, Status Report 1993, DESY 1993.
[2] W. Buchmüller *et. al.*, Phys. Lett. **B191** (1987) 442.
[3] W. Buchmüller, Phys. Lett. **B177** (1986) 377.
[4] S. Davidson *et. al.*, Z. Phys. **C61** (1994) 613.
[5] M. Leurer, Phys. Rev. Lett. **71** (1993) 1324, Phys. Rev. **D49** (1994) 333, Phys. Rev. **D50** (1994) 536.
[6] I.I. Bigi *et. al.*, Phys. Lett. **B166** (1986) 238.
[7] G. Ingelman, T. Sjöstrand, Lund Preprint LU TP 80-12. G. Ingelman, LEPTO version 6.1, Proc. of the HERA Workshop **V3** (1991) 1366.
[8] A. Kwiatkowski *et al.*, Proc. of the HERA Workshop **V3** (1991) 1294.
[9] L. Lönnblad, Proc. of the HERA Workshop **V3** (1991) 1440.
[10] B.R. Webber *et al.*, Computer Phys. Comm. **67** (1992) 465.
[11] A.D. Martin *et al.*, Phys. Rev. **D47** (1993) 867.
[12] M. Glück, E. Reya, A. Vogt, Phys. Rev. **D46** (1992) 1973.
[13] H.U. Bengtsson, T. Sjöstrand, Computer Phys. Comm. **46** (1987) 43. **Pythia** was modified to produce νq, μc, and τb final states in addition to eq.
[14] A. Andresen *et al.*, Nucl. Inst. Meth. **A309** (1991) 101, A. Bernstein *et al.*, Nucl. Inst. Meth. **A336** (1993) 23, A. Caldwell *et al.*, Nucl. Inst. Meth. **A321** (1992) 356.
[15] C.B. Brooks *et al.*, Nucl. Instr. Meth. **A283** (1989) 477, B. Foster *et al.*, Nucl. Instr. Meth. **A338** (1994) 254.
[16] C. Alvisi *et al.*, Nucl. Instr. Meth. **A305** (1991) 30.